CONTRAST ENHANCED MRI FOR THE MEASUREMENT OF DYNAMIC SIGNAL CHANGES IN THE CSF AND CEREBRAL LYMPHATIC VESSELS

by
Di Cao

A dissertation submitted to Johns Hopkins University in conformity with the requirements for the degree of Doctor of Philosophy

Baltimore, Maryland

September 2022

Abstract

Cerebrospinal fluid (CSF) circulation is critical for waste clearance from the brain parenchyma. Dysfunction of the system has been linked to abnormal protein deposition in patients with Alzheimer's (Aβ, tau) and Parkinson's (alpha-synuclein) disease. The cerebral lymphatic vessels communicate with routes for CSF circulation and are believed to play a crucial role in the drainage of CSF from brain tissues to cervical lymph nodes. The study of CSF flow in cerebral lymphatic vessels can provide critical information regarding the clearance of abnormal proteins and metabolites from brain tissues. Accumulating evidence has indicated the importance of studying the interaction between the microvascular and lymphatic systems in the brain.

Contrast-enhanced MRI is currently the most promising method for imaging CSF flow in the cerebral lymphatic vessels in humans. However, as most existing human MRI scans take > 5 minutes, the temporal resolution is poor for tracking dynamic changes in these vessels. The first contribution of this thesis is the development of MRI techniques for the measurement of dynamic susceptibility contrast changes in CSF (cDSC) in the human brain. With the cDSC method developed in this thesis, dynamic signal changes after Gd injection in the CSF can be detected at several locations where cerebral lymphatic vessels were identified in previous studies. The concentration of Gd in CSF in these regions was estimated to be approximately 0.2 mmol/L.

To date, most imaging methods can only measure blood or lymphatic vessels separately. The second contribution of this thesis is that we further expanded the MRI method for simultaneously dynamic imaging of small blood and lymphatic vessels in the

human brain with dynamic dual-spin-echo perfusion (DDSEP) MRI. The proposed DDSEP method showed consistent results in human brains as previous studies using separate methods. To the best of our knowledge, this may be the first study in which the temporal difference in Gd-induced signal changes from small blood and lymphatic vessels after intravenous Gd-injection was measured in the same human subjects.

Primary Reader and Advisor: Jun Hua
Secondary Reader: Vikram Chib

Acknowledgements

I am very grateful to my advisor, Professor Jun Hua, for his guidance along my PhD study. I am thankful to him for his patient guidance and constant encouragement for giving me the freedom to explore new research ideas, which not only helped me to shape my independent research interests but also made the research process enjoyable. He has also taught me many important and precious lessons in life which will be my life-long treasure. All in all, I consider myself super lucky to be his student.

I am also grateful to Prof. Hanzhang Lu, Prof. Vikram Chib, for serving in my thesis proposal and dissertation committees and for their valuable suggestions on my thesis.

I would like to thank my lab mates: Adrian Paez, Xinyuan Miao, Chunming Gu, Yinghao Li, and Yuanqi Sun for supportive help during my PhD research. I also want to express my huge thanks to Dapeng Liu for tremendous help answering my questions during early stage of my PhD.

I would like to thank Mr. Joseph S. Gillen, Mrs. Terri Lee Brawner, Ms. Kathleen A. Kahl, and Ms. Ivana Kusevic for experimental assistance during my PhD research.

Finally, I also want to thank my partner: Yixin Ma. Thanks for your continuous support and accompany.

Dedication

This thesis is dedicated to my parents, Yuanbao Cao and Xiuqin Xie, for their eternal love, trust and support.

Contents

List of Tables

List of Figures

Chapter 1

1. Introduction

1.1 CSF and cerebral lymphatic vessels

Cerebrospinal fluid (CSF) is a clear fluid that exists in the surrounding spaces of central nervous systems (CNS). The circulation of CSF influences various aspects of brain physiology, including substance distribution and waste clearance from the brain parenchyma. Dysfunction of the CSF system has been linked to abnormal protein deposition in patients with Alzheimer's and Parkinson's disease.

There is about 125–150 mL of CSF in the human brain (1). The majority of CSF is produced by choroid plexus within the ventricles. From here, CSF passes through the interventricular foramina to the third ventricle, and then circulates from the third ventricle to the fourth ventricle through the cerebral aqueduct. From the fourth ventricle, the fluid passes into the subarachnoid space in a single outward direction. But CSF flows multidirectionally in the subarachnoid space (2). Fluid movement of CSF is pulsatile, driven by the arterial pulsation wave generated in blood vessels in brain parenchyma.

From the subarachnoid space, there are two pathways for CSF egress from the brain. One is that CSF goes into veins directly through arachnoid granulation. More

recently, another pathway has been proposed, which involves the lymphatic vessels in the dural matter. These lymphatic vessels may play a critical role in the clearance of CSF.

For the last few decades, lymphatic vessels were thought to be absent in the central nervous system. Recently, cerebral vessels with typical endothelial markers as lymphatic vessels in other organs in the body have been identified in the dura mater alongside the dural venous sinuses, in regions around the middle meningeal artery and cribriform plate (3-5), and in the basal part of the skull (6) in animal models. Some of the meningeal lymphatic vessels have also been visualized in human brains (5). Cerebral lymphatic vessels are believed to play an important role in the drainage of CSF into the cervical lymph nodes (3,4,7-12), which has intriguing clinical implications for the clearance of abnormal protein and other products in many brain diseases such as Alzheimer's disease and Parkinson's disease.

1.2 Contrast enhanced MRI to measure brain perfusion

1.2.1 DSC/DCE MRI for blood perfusion

Contrast enhanced (CE) MRI techniques, including dynamic susceptibility contrast (DSC) MRI and dynamic contrast enhancement (DCE) MRI have been widely used in clinical and research studies (13,14). Currently, intravenous (IV) administration of gadolinium(Gd)-based contrast medium is the only FDA approved approach for human studies in the US and the most commonly used method worldwide. CE MRI has been mainly used for measuring Gd-induced MR signal changes from the blood (13).

DSC MRI is a standard perfusion technique performed routinely in clinical MRI (13,14). DSC MRI can measure several key parameters reflecting the function and

integrity of blood vessels, such as cerebral blood flow (CBF) and volume (CBV), and blood brain barrier (BBB) permeability. In typical DSC MRI experiments, MR images are continuously acquired before, during and after intravenous (IV) administration of Gadolinium (Gd) based contrast agents with a few seconds temporal resolution, generating a response time course. Then, microvascular parameters can be derived from time course.

DCE MRI is another CE MRI technique which also requires administration of a gadolinium-based contrast agent. DCE MRI exploits the T1 shortening effects of gadolinium, acquiring repeated T1-weighted images over an approximately 5-10 minutes interval with a relative lower temporal resolution. Form the time course, full quantification can be obtained by applying a compartmental model allowing several physiological parameters to be derived, including the transfer constant (K^{trans}), fractional plasma volume (v_p), and fractional volume of the tissue extracellular space (v_e).

1.2.2 Existing MRI methods for cerebral lymphatic vessels

In addition, it is also well known that pre- and post-Gd MR signal difference are often detected in the CSF at several locations within the intra-cranial space (15-18). This has been attributed to the fact that the dural blood vessels do not have a BBB as cortical blood vessels, and thus some Gd-based contrast agents can cross the dural blood vessel wall and enter the CSF circulation.

As Gd-based contrast agents significantly shorten T1 and T2 values of the CSF and interstitual fluid (ISF), both T1-weighted and T2-weighted MRI sequences can be employed to detect the pre- and post-Gd MR signal changes in the CSF and ISF. As IV

administration is still the predominant procedure for Gd-based contrast agents, one important requirement for these sequences is to separate signal changes from the blood and the CSF/ISF. T1-weighted fast gradient-echo (GRE) sequences are commonly used in various human and animal studies (6,19-23,30-36). These sequences have been widely used in conventional DCE MRI for blood perfusion (13). One potential caveat is that the extravascular effects are substantial in GRE sequences even with short echo time (TE), which can lead to some uncertainty on whether the MR signal changes are originated from the CSF space or the nearby small blood vessels. To improve the spatial specificity especially for small perivascular space or cerebral lymphatic vessels, T1-weighted fast spin-echo (FSE) sequences have been used in some studies (10,20,35,37). The extravascular effects are much smaller in spin-echo based sequences compared to GRE sequences (38,39). T1-weighted sequences usually have a short repetition time (TR), making it highly time efficient. However, both blood and CSF/ISF show significant post-Gd signal changes in T1-weighted sequences, which may result in substantial partial volume effects. To reduce such partial volume effects from blood, T2-weighted FSE sequences with a long TE have been proposed for imaging Gd-induced signal changes in the CSF (37,40). Because the T2 value of CSF is at least one order longer (~ 1000 ms for CSF, and less than 100 ms for blood) than that of blood, a sufficiently long TE can almost completely suppress blood and tissue signals due to T2 decay, leaving CSF the only compartment that is detectable in the resulting T2-weighted images. One disadvantage of T2-weighted sequences is that it often requires a long TR, which limits its time efficiency. Another type of sequences commonly adopted is inversion recovery based sequences such as fluid-attenuation inversion recovery (FLAIR) (5,6,32,35,41-43) and black blood (5) MRI, which use inversion recovery to suppress CSF/ISF and blood signals, respectively.

Whilst the inversion recovery technique can often generate stronger contrast for Gd-induced signal changes in the CSF, it also introduces a long inversion recovery period which may limit its temporal resolution. Using FLAIR and black blood MRI with IV Gd administration, Absinta et al. demonstrated that meningeal lymphatic vessels can be visualized in the human brain and validated their MRI results with histology (5). One important point to consider when interpreting Gd-induced MR signal changes is that the concentration of Gd-based contrast agents can have dramatic effects on the observed post-Gd signal changes. Depending on the pulse sequences and imaging parameters applied, hyperintensities or greater post-Gd signal changes do not always correspond to higher Gd concentration. It has been shown that MR signal changes, especially from T1-weighed sequences, can have a biphasic relationship with Gd concentration (40,44). Therefore, it is critical to understand the relationship between the expected Gd-induced signal changes and Gd concentration when choosing MRI sequences and imaging parameters for particular studies. Note that the Gd concentration can be very different for various Gd-based contrast agent injection procedures. All the sequenced discussed so far typically take 5-10 minutes to achieve whole brain coverage and sufficient spatial resolution for imaging the CSF space, perivascular space, and cerebral lymphatic vessels in the human brain. The temporal resolution is relatively low compared to typical DSC and DCE MRI for blood perfusion in the brain. Although the CSF circulation is much slower than the blood circulation, it may still be useful for certain studies especially with IV injection of Gd-based contrast agents to track the dynamic signal changes in the CSF and cerebral lymphatic vessels with a better temporal resolution.

1.3 Thesis contributions

The CSF space can be visualized on structural MR images with proper contrast adjusted to the much longer longitudinal (T1) and transverse (T2) relaxation times of CSF compared to the other tissues in the brain. When gadolinium(Gd)-based contrast medium are used, MR signal contrast between pre-contrast and post-contrast MR images can often be observed in the CSF at certain locations within the intra-cranial space (15-18). This is mainly due to the fact that the dural blood vessels lack a blood-brain barrier (BBB) that presents in cortical blood vessels, which enables some of the commonly used Gd contrast agents in human clinical MRI scans to cross the dural blood vessel wall and to enter the CSF. Recent studies have shown that some meningeal lymphatic vessels in the brain can be visualized using MRI with Gd contrast in human brains (5). Furthermore, if the dynamic signal changes in the CSF and cerebral lymphatic vessels before and after Gd administration can be tracked with sufficient spatial and temporal resolution, it may serve as a useful tool for the investigation of CSF drainage routes in the brain, which has not been fully understood yet. To detect the Gd-based MR signal changes in the CSF and cerebral lymphatic vessels, most studies to date adopt inversion recovery based sequences such as fluid-attenuation inversion recovery (FLAIR) and black blood MRI (5,41), or fast gradient-echo (GRE) sequences (19-23,30-34).

Contrast-enhanced MRI is currently the most promising method for imaging CSF flow in the cerebral lymphatic vessels in humans. However, as most existing human MRI scans take > 5 minutes, the temporal resolution is poor for tracking dynamic changes in these vessels. The first contribution of this thesis is the development of MRI techniques for the measurement of CSF dynamic susceptibility contrast changes (cDSC) in small

lymphatic vessels in human brain. With the cDSC method developed in this thesis, dynamic signal changes after Gd injection in the CSF were detected at several locations where cerebral lymphatic vessels were identified in previous studies. The concentration of Gd in CSF in these regions was estimated to be approximately 0.2 mmol/L.

To date, most imaging methods can only measure blood or lymphatic vessels separately. The second contribution of this thesis is that we further expanded the MRI method for simultaneously dynamic imaging of small blood and lymphatic vessels in the brain with dynamic dual-spin-echo perfusion (DDSEP) MRI. The proposed DDSEP method showed consistent results in human brains as previous studies using separate methods. To the best of our knowledge, this may be the first study in which the temporal difference in Gd-induced signal changes from small blood and lymphatic vessels after intravenous Gd-injection was measured in the same human subjects.

Chapter 2

2. Technical preparation: evaluation of parallel imaging methods in MRI

2.1 Introduction

Parallel imaging methods can significantly speed up MRI data acquisition, which has a fundamental impact on the application of various MRI sequences (45). The SENSitivity Encoding (SENSE) technique (46) utilizes the sensitivity information from multi-channel receiver array coils to reconstruct under-sampled data, and has become one of the most commonly used parallel imaging methods on modern clinical MRI systems. Recently, the Compressed Sensing-Sensitivity Encoding (CS-SENSE) technique (47) has been developed. CS-SENSE combines the original SENSE technique with the transform sparsity and compression theory from the Compressed Sensing (CS) framework to achieve greater acceleration with less penalties on image quality (48).

Many independent studies have conducted to evaluate the performance (mainly the signal-to-noise ratio, or SNR) in CS-SENSE with acceleration factors (R) of 2-8. CS-SENSE with R = 2-8 showed comparable data quality as the fully sampled acquisitions in studies using 3D cine phase contrast MRI (R=7) (49), MR spectroscopy imaging (R=4)

(50), T2-weighted volume isotropic turbo spin echo acquisition (VISTA) and contrast enhanced 3D T1-weighted turbo Field echo (TFE) (R=2) (51), Chemical exchange saturation transfer (CEST) MRI (R=4) (52), Gadoxetic acid-enhanced dynamic MRI (R=3.4) (53), T1-weighted dual echo Dixon hepatobiliary phase imaging (R=4.5) (54), 4D flow cardiovascular MR (R=6-8) (55), and functional MRI (R=4) (56). CS-SENSE also demonstrated better performance than SENSE with the same R of 2-8 in studies using T2 VISTA (57) and contrast enhanced 3D T1 TFE (R=2) (51), variants of multi-echo gradient-echo imaging of the liver (R=4) (58), whole-heart MR angiography (R=6) (59), vessel high resolution MRI T1-weighted (R=6.8) and proton density (R=5.8) (60). To date, however, most studies focused on the assessment of CS-SENSE with R<8 using the SNR as the primary outcome measure.

In this study, we attempt to evaluate and compare the performance of CS-SENSE and SENSE with high acceleration factors (R) up to 28 in order to further push the limit for temporal and spatial resolution in MRI sequences using CS-SENSE and SENSE. In addition to SNR, the point-spread-functions (PSF) in each sequence was measured to evaluate the spatial blurring artifacts induced by under-sampling and denoising algorithms in CS-SENSE and SENSE. Two commonly used 3D MRI sequences were evaluated: the T1-weighted Magnetization Prepared RApid Gradient Echo (MPRAGE), and the T2-weighted Turbo Spin Echo (TSE, also known as fast spin echo or FSE) sequences. Higher R is expected to be beneficial in these sequences to achieve whole-brain coverage with ideal spatial resolution and to reduce power deposition from the readout train (especially 3D TSE). As the readout echo train length has a fundamental effect on PSF and SNR especially in 3D TSE, two 3D TSE sequences with short (300ms) and long (2800ms) echo trains were evaluated. The short-echo-train 3D TSE sequence is often used for T2-

weighted anatomical imaging, whereas the long-echo-train 3D TSE sequence can be a useful method for imaging the cerebrospinal fluid (CSF) space (61). SNR and PSF in each sequence were experimentally measured on phantoms and human brains with R ranging from 0 to 28. The results from this study are expected to provide a practical guideline for the choice of imaging parameters in 3D MPRAGE and TSE sequences with high CS-SENSE and SENSE acceleration factors.

2.2 Materials and Methods

All experiments were performed on a 3T Philips human MRI scanner (Philips Healthcare, Best, The Netherlands) with a 32-channel head coil array (Nova Medical, Wilmington, MA) for signal reception and a dual-channel body coil for transmission.

2.2.1 MRI pulse sequences acquisition

Three pulse sequences were evaluated in this study with the following parameters:

1) T1-weighted 3D MPRAGE: repetition time (TR)/echo time (TE)/inversion time (TI) = 8.1/3.7/818ms, echo train duration = 1500ms, shot interval = 3000ms, field of view (FOV) = 210x184mm^2, voxel = 1mm isotropic, 130 slices;

2) T2-weighted 3D TSE with a short echo train: TR/TE/echo spacing (ES) = 3000/150/6ms, echo train duration = 300ms, TSE factor = 50, FOV = 210x184mm^2, voxel = 1mm isotropic, 130 slices;

3) T2-weighted 3D TSE with a long echo train: TR/TE/ES=9000/1409/4.5ms, echo train length = 2800ms, TSE factor = 620, FOV = 210x184mm^2, voxel = 0.75mm isotropic, 173 slices. The voxel size in this sequence was slightly smaller than sequences 1) and 2). It was chosen based on our cDSC method in chapter 3(61). Comparisons of PSF and

SNR were conducted within each sequence with varying R. No comparisons between these three sequences were performed.

Each sequence was performed using CS-SENSE or SENSE with R = 0, 2, 4, 6, 8, 10, 12, 16, 20, 28. Note that both CS-SENSE and SENSE were performed in 2D mode (for 3D sequences) using acceleration in two phase-encoding directions (RL and FH) simultaneously. The maximum acceleration factor R is limited by the number of channels (32-channel) in the receiving head coil array. Scan durations of each sequence performed with different R are listed in **Table 1**.

Table 1: Scan duration for each sequence with varying acceleration factors

Acceleration factor (R)										
	R=0	**R=2**	**R=4**	**R=6**	**R=8**	**R=10**	**R=12**	**R=16**	**R=20**	**R=28**
CS-SENSE	0	2	4	6	8	10	12	16	20	28
SENSE (RLxFH)	0	2x1	2x2	3x2	4x2	4x2.5	4x3	4x4	5x4	7x4
Volume TR (min:sec)										
3D MPRAGE	04:50	02:30	01:15	00:51	00:36	00:30	00:23	00:18	00:15	00:09
Short echo train 3D TSE	18:45	09:39	04:51	03:15	02:24	01:57	01:36	01:12	00:57	00:47
Long echo train 3D TSE	07:57	04:03	01:57	01:21	00:54	00:45	00:36	00:27	00:18	00:09

In addition, the denoising level, a key parameter that controls the denoising filter strength in CS-SENSE reconstruction algorithm implemented by the vendor on our scanner, was also varied and evaluated. Effects from four different denoising levels: 0%,

10%, 15% (default setting on the scanner), and 30% were assessed by performing the MRPAGE sequence with R = 2, 10, and 28 and these denoising levels. All the other sequences described above were performed with the default denoising level (15%).

2.2.2 Phantom and human studies design

Two phantoms of comparable sizes of the human brain were constructed for this study:

1) A bottle phantom (length = 20 cm, diameter = 15cm) containing 3000 cc Spectrasyn 4 (oil): The T1 and T2 values of this phantom were measured to be approximately 1400ms and 60ms, respectively, which are comparable to those of grey matter (GM) and white matter (WM) in human brains. The MPRAGE and short-echo-train TSE sequences were evaluated using this phantom;

2) A sphere phantom (diameter = 18 cm) containing tap water to mimic the T1 and T2 of CSF: This phantom was used to evaluate the long-echo-train TSE sequences.

Each sequence was performed twice on phantoms. First, the PSF of each scan was measured using the one-dimensional Fourier transform (1D-FT) mode provided by the vendor (Philips) on the two phase-encoding directions (RL and FH) when the gradients in corresponding directions are disabled. The 3D k-space data acquired without phase-encoding gradients condense into 1D along the center of the FOV along the phase-encoding directions. In the ideal case where no blurring effect is induced by the reconstruction algorithm, reconstructing this 1D k-space data should lead to an infinitely thin line in the readout direction (AP). In reality, the blurring effects caused by the reconstruction algorithm can be measured by the PSF on each direction. Second, the

same sequences were repeated with the normal imaging mode to assess SNR in the MR images from each scan.

All imaging sequences were performed on three healthy human subjects (one female, two males; age 23-28 years). The study was approved by the Johns Hopkins Institutional Review Board, and written informed consent was obtained from each participant.

2.2.3 Data analysis: PSF and SNR measurement

Full-width-at-half-maximum (FWHM) was calculated from the measured PSF on each phase encoding direction. SNR was calculated from the MR images as the mean signal divided by the standard deviation, and SNR per-unit-time was obtained by normalizing SNR by the square root of acquisition time per slice (in seconds). In phantom scans, a region-of-interest (ROI) was manually drawn to cover most of the phantom on all slices. In human scans, an ROI was manually drawn to cover most of the WM region on ten consecutive slices in the MRPAGE and short-echo-train TSE scans; and to cover most of the ventricle (CSF) region in the long-echo-train TSE scans. The ROIs were kept identical for each subject in all sequences. Both FWHM and SNR values were averaged over ten slices in readout direction with mean square errors reported as well.

2.3 Results

2.3.1 PSF with different acceleration factors

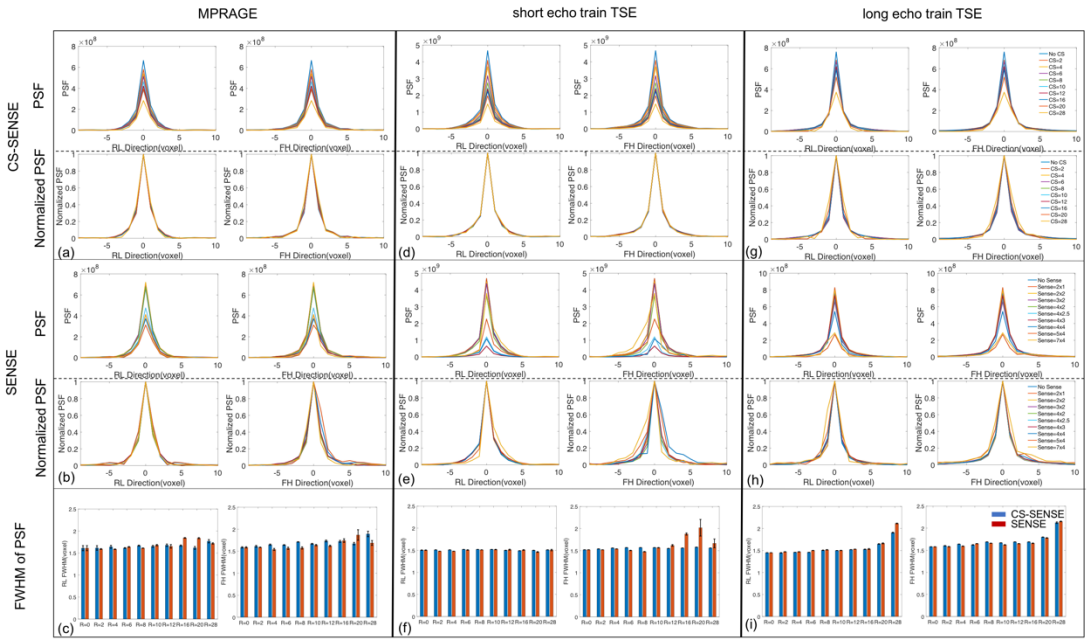

Figure 1: PSF of SENSE and CS-ENSE measurement in phantom: PSF, normalized PSF and FWHM of PSF in two phase encoding directions (RL, FH) measured from the MPRAGE (A,B,C), short echo train TSE (D,E,F) and long echo Train TSE (G,H,I) sequences with various accelerations factors (R).

Figure 1 shows the PSFs measured in phantoms for each sequence (MPRAGE, short-echo-train TSE, and long-echo-train TSE) using different acceleration factors in CS-SENSE or SENSE. Both the original PSF and the PSF normalized by its peak were shown for each scan. The peaks of the original PSFs decreased as R increased in each sequence, indicating decreasing SNR as expected (see next section). In all three sequences, no significant difference in the FWHM of PSF was found between corresponding CS-SENSE and SENSE scans with the same R (R<16). The FWHM of PSF remained approximately constant (1.5-1.7 voxels) in both phase-encoding directions (RL and FH) for R<16 as

compared to the corresponding scans without acceleration (R=0), and slightly increased to 1.7-1.9 voxels for R>20 in all three sequences.

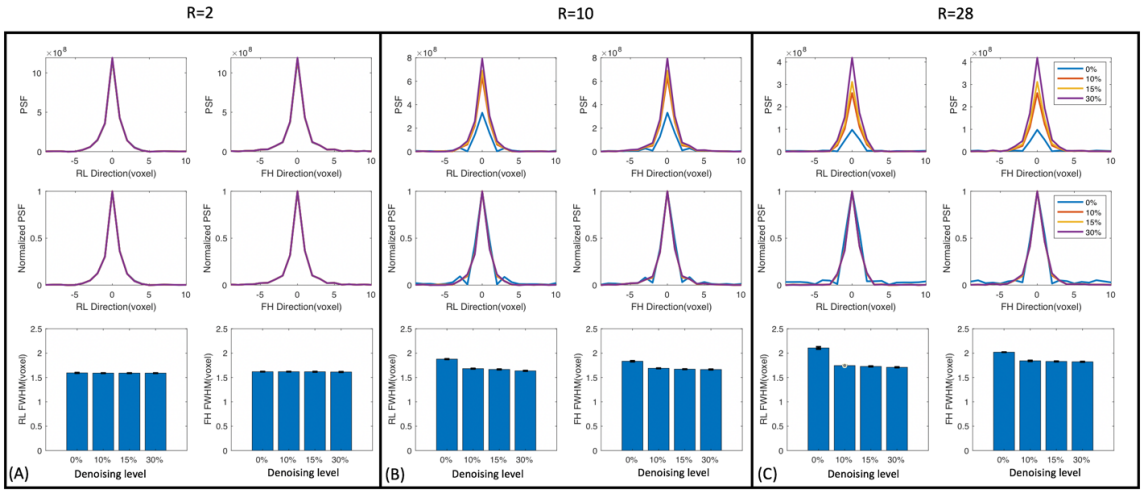

Figure 2: PSF of MPRAGE with CS-SENSE with different denoising levels. Four different denoising levels (no (0%), weak (10%), median (15%, default setting on the scanner) and strong (30%)) in CS-SENSE were evaluated using the MPRAGE sequence with R = 2 (A), 10 (B), and 28 (C). PSF, normalized PSF and FWHM of PSF in two phase encoding directions (RL, FH) were shown for each sequence.

Figure 2 shows the measured PSFs and their FWHM with different CS-SENSE denoising levels for the MPRAGE sequence at R=2, 10 and 28. The FWHM of PSF in both phase-encoding directions in the scans with 0% denoising level were slightly higher than those in scans with denoising levels of 5%, 15% and 30% at R=10 and R=28. No significant difference in FWHM was observed among scans with 5%, 15% and 30% denoising levels.

2.3.2 SNR results with different acceleration factors

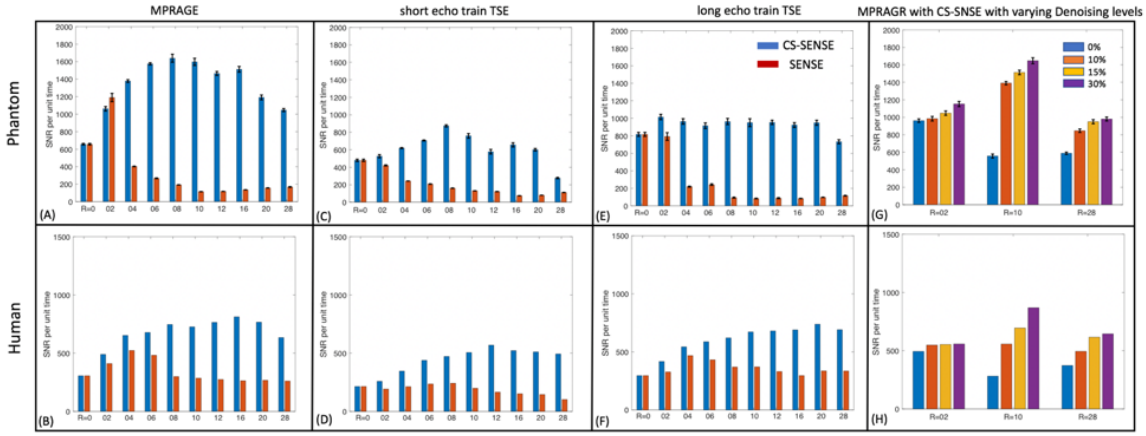

Figure 3: Measured SNR per-unit-time resultsin phantom (A, C, E, G) and human scans (B, D, F, H). SNR per-unit-time was compared between CS-SENSE and SENSE with R ranging from 0 to 28 for MPRAGE (A, B), short echo train (C, D) and long echo train (E, F) 3D TSE sequences. (G, H) compare SNR per-unit-time in the MPRAGE sequence using CS-SENSE with four different denoising levels (0%, 10%, 15%, 30%).

Figures 3(A-F) compare the measured SNR-per-unit-time from all sequences in both phantom and human scans with varying R. In phantom scans (**Figures 3(A,C,E)**), CS-SENSE showed comparable SNR-per-unit-time as SENSE for R=0 and 2, but significantly greater (73-89%) SNR-per-unit-time for R>=4 ($P<0.01$) in all three sequences. In human scans (**Figures 3(B,D,F)**), CS-SENSE showed comparable or slightly higher SNR-per-unit-time compared to SENSE for R=0, 2 and 4, but significantly greater (32-78%) SNR-per-unit-time for R>=6 ($P<0.01$) in all three sequences. In CS-SENSE, SNR-per-unit-time preserved when R increased from 0 to 28, as shown in all three sequences performed on phantoms and human brains. On the other hand, SNR-per-unit-time in SENSE started to drop significantly when R increased to 4 in phantom scans, and when R increased to 6-10 in human brain scans. **Figures 3(G,H)** compare SNR-per-unit-time in MPRAGE scans with different denoising levels in CS-SENSE performed with R=2, 10, and

28 on phantoms and human brains. As expected, SNR-per-unit-time became higher with a stronger denoising level for both phantom and human scans.

2.3.3 Human brain images with different acceleration factors

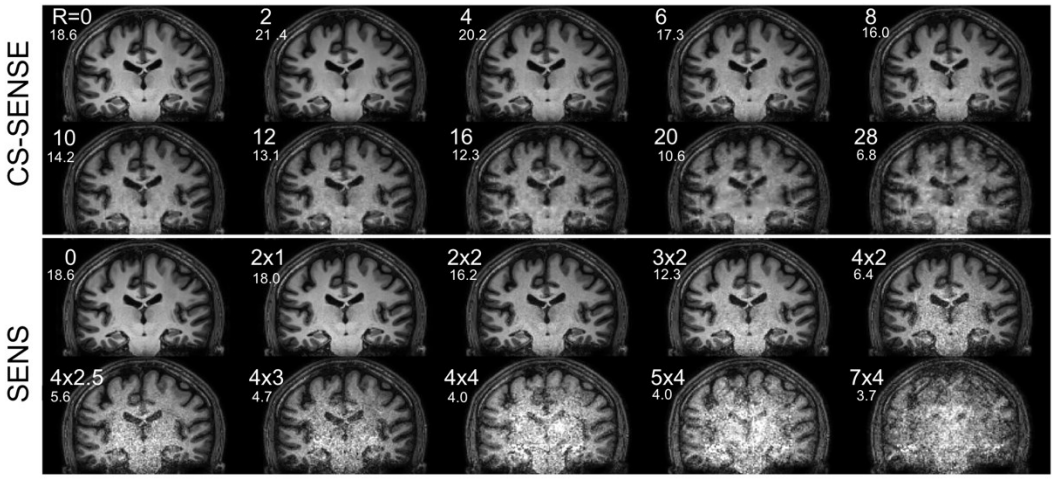

Figure 4: Typical human brain images acquired using the MPRAGE sequences. One coronal slice was shown for each scan performed with CS-SENSE or SENSE with R from 0 to 28 (marked at the top left corner of each image) and default denoising level (15%) in CS-SENSE. The scale was kept identical for all images. The SNR for each scan (not SNR per-unit-time) was shown at the top left corner of each image.

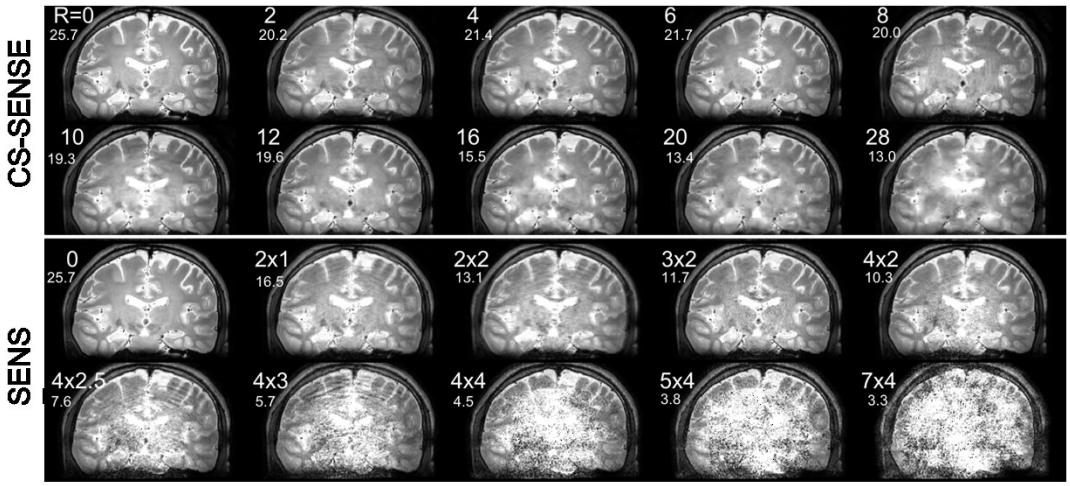

Figure 5: Typical human brain images acquired using the short echo train 3D TSE sequenceswith CS-SENSE or SENSEfor R from 0 to 28 are shown. Default denoising level (15%) was used in CS-SENSE. Corresponding R and SNR (not SNR per-unit-time) of each image are shown at top left corner of each image. The scale was kept identical for all images.

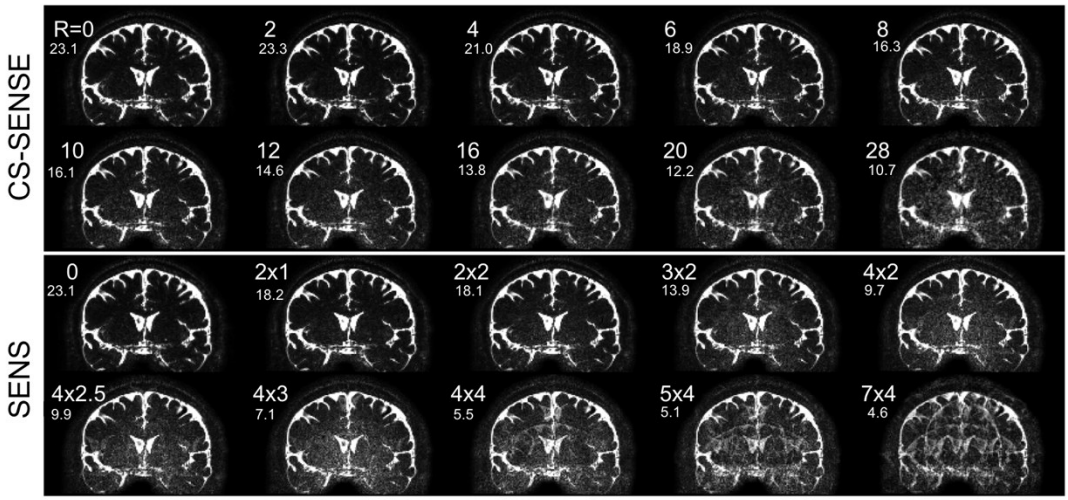

Figure 6: Typical human brain images acquired using the long echo train 3D TSE sequenceswith CS-SENSE or SENSEfor R from 0 to 28 are shown. Default denoising level (15%) was used in CS-SENSE. Corresponding R and SNR (not SNR per-unit-time) are shown at top left corner of each image. The scale was kept

identical for all images. There are noticeable fold-over artifacts for SENSE with R>8.

Typical human brain images acquired using MPRAGE, short-echo-train TSE and long-echo-train TSE sequences with CS-SENSE or SENSE with varying R are shown in **Figures 4**-**6**. Note that each image here was from a single acquisition with each sequence. Therefore, the acquisition time (volume TR) became shorter with higher acceleration (larger R, listed in **Table 1**). The SNR from the single acquisition (not SNR-per-unit-time) was listed on each image, which decreased with increasing R in both CS-SENSE and SENSE. Nevertheless, CS-SENSE showed better image quality than SENSE with the same R in all three sequences, especially with R>8. CS-SENSE did not show obvious foldover artifacts in all three sequences with R=0-28, whereas SENSE showed substantial foldover artifacts with R>8, which were especially prominent in long-echo-train TSE images (**Figure 6**). **Figure 7** shows a comparison of human brain image quality in MPRAGE scans with different denoising levels in CS-SENSE with R=2, 10, and 28. The image quality and SNR increased with stronger denoising level as expected for all R values.

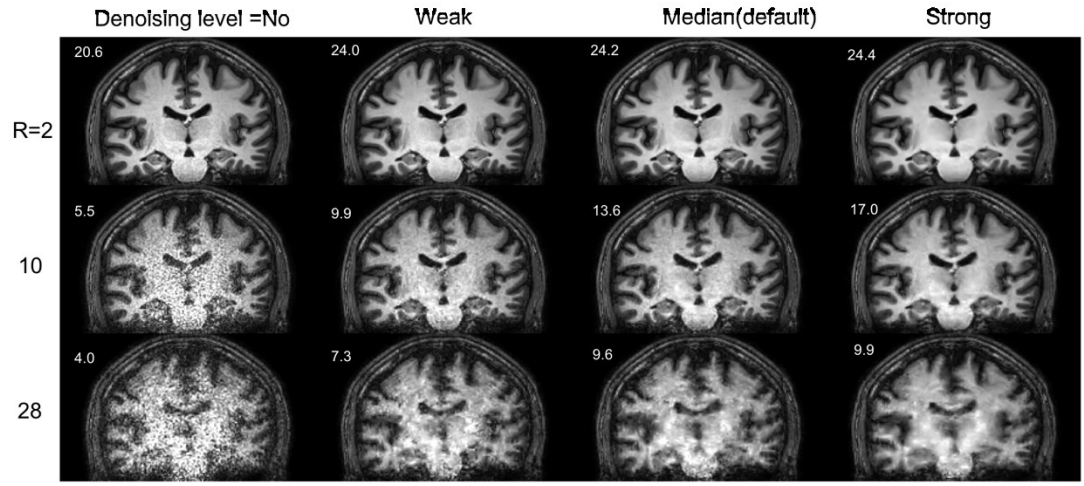

Figure 7: Typical human brain images acquired using the MPRAGE sequence with CS-SENSE with varying denoising levelsare shown. Four different denoising levels (0%, 10%, 15% and 30%) with three different R = 2, 10, and 28 were used to evaluate the image quality. The corresponding SNR (not SNR per-unit-time) is shown at top left corner of each image. The scale was kept identical for all images.

2.4 Discussion

This study compared the CS-SENSE and SENSE parallel imaging techniques in highly accelerated 3D MPRAGE and TSE sequences performed on phantoms and human brains. While most previous studies focused on the evaluation of the SNR of MR images acquired using CS-SENSE and SENSE with acceleration factors up to 8, the current study attempted to further push the limit and to assess their performance by measuring both the PSF and SNR of the images acquired with acceleration factors up to 28. The PSF results demonstrated that the spatial blurring effects were similar in CS-SENSE and SENSE, and there was little blurring effect in both CS-SENSE and SENSE with R<16 (comparable FWHM of PSF as the corresponding scans without acceleration, i.e. R=0). Both CS-SENSE and SENSE with under-sampling k-space data acquired enough high frequency

component (R<16) to maintain the same resolution as full-sampling data until extremely high under-sampling(R>20) in which the largely missing high frequency component may induce blurring effect. Note that the measured PSFs in the MPRAGE sequences were similar in the two phase encoding directions (RL and FH) because radial phase encoding trajectory was used in the MPRAGE sequences. On the other hand, as linear phase encoding trajectory was used in the TSE sequences, the FWHM of PSF of the second phase encoding direction (FH) was larger than that of the first phase encoding direction (RL) because of the blurring effects induced by T2 decay along the second phase encoding direction.

CS-SENSE showed superior SNR measured in both phantoms and human brains than SENSE especially for R>=6. There are two reasons to explain this. First, CS-SENSE contains a compressed sensing component in the reconstruction which will remove the noise and increase the SNR. Second, SENSE has the foldover artifact (R>4) which will increase the standard deviation of ROI and reduce SNR dramatically especially on phantom scans. Note that all ROIs drown on phantoms contain the location of foldover artifact. However, ROIs drown on human image may missed location of foldover artifact. That's why SNR of SENSE on phantom drops faster than SNR of SENSE in human scan. CS-SENSE still has much higher SNR compared with SENSE in human scan even without considering of foldover artifact.

CS-SENSE did not show visible foldover artifacts even with high R up to 28, while foldover artifacts were evident in SENSE images when R in one phase-encoding direction was larger than 4. Foldover artifact is more obvious in phantom scans and long echo train TSE (CSF imaging) on human scans since foldover artifact is more visible in sparsity image compared to complicated structure image.

The performance of parallel imaging techniques is limited by the MRI scanner hardware especially the receiving array. In this study, the highest R tested was 28, which was limited by the number of channels in the receiving head coil. The 32-channel head coil is now available on most state-of-the-art clinical 3T MRI systems. With the further development of MRI hardware, head coil arrays with more receiving channels (64-128) are expected to allow higher acceleration factors in parallel imaging using CS-SENSE and SENSE.

Two commonly used MRI sequences were evaluated in the current study: the 3D MPRAGE and TSE sequences, which are widely used as T1-weighted and T2-weighted anatomical MRI scans, respectively. In addition, these sequences have been applied in various other MRI sequences. For instance, the 3D fast-gradient-echo (GRE) readout in MPRAGE is often used in susceptibility weighted imaging (SWI). The 3D GRE readout and the 3D TSE sequence can be used as the readout modules in many MRI sequences with spin preparation modules, such as fluid-attenuated inversion recovery (FLAIR), arterial spin labeling (ASL), MR angiography (MRA), CEST, vascular-space-occupancy (VASO) (62), and spin-prepared functional (63) and diffusion (64) MRI sequences. Besides the brain, 3D fast GRE and TSE are also extensively applied in imaging other organs, such as cardiac and liver MRI. Therefore, the results from this study may provide useful information for studies using a wide range of MRI sequences.

In summary, CS-SENSE showed superior SNR than SENSE in MPRAGE and TSE scans performed with high acceleration factors (R=0-28) on phantoms and human brains. The spatial blurring effects evaluated by the FWHM of PSF were comparable between CS-SENSE and SENSE and were negligible for R<=16. Significant foldover artifacts only

occurred in SENSE images. Based on these results, CS-SENSE appears to be the favored parallel imaging technique compared to SENSE, and the acceleration factor R can be pushed up to around 16 for highly accelerated acquisitions with a 32-channel receiver array coil.

Chapter 3

3. Dynamic susceptibility contrast changes in the CSF (cDSC) MRI

3.1 Introduction

The circulation of cerebrospinal fluid (CSF) influences various aspects of brain physiology, including substance distribution and waste clearance from the brain parenchyma. Recently, cerebral vessels with typical endothelial markers as lymphatic vessels in other organs in the body have been identified in the dura mater alongside the dural venous sinuses, in regions around the middle meningeal artery and cribriform plate (3-5), and in the basal part of the skull (6) in animal models. Some of the meningeal lymphatic vessels have also been visualized in human brains (5). Cerebral lymphatic vessels are believed to play an important role in the drainage of CSF into the cervical lymph nodes (3,4,7-12), which has intriguing clinical implications for the clearance of abnormal protein and other products in many brain diseases such as Alzheimer's disease and Parkinson's disease.

The CSF space can be visualized on structural MR images with proper contrast adjusted to the much longer longitudinal (T1) and transverse (T2) relaxation times of CSF

compared to the other tissues in the brain. When gadolinium(Gd)-based contrast medium are used, MR signal contrast between pre-contrast and post-contrast MR images can often be observed in the CSF at certain locations within the intra-cranial space (15-18). This is mainly due to the fact that the dural blood vessels lack a blood-brain barrier (BBB) that presents in cortical blood vessels, which enables some of the commonly used Gd contrast agents in human clinical MRI scans to cross the dural blood vessel wall and to enter the CSF. Recent studies have shown that some meningeal lymphatic vessels in the brain can be visualized using MRI with Gd contrast in human brains (5). Furthermore, if the dynamic signal changes in the CSF and cerebral lymphatic vessels before and after Gd administration can be tracked with sufficient spatial and temporal resolution, it may serve as a useful tool for the investigation of CSF drainage routes in the brain, which has not been fully understood yet. To detect the Gd-based MR signal changes in the CSF and cerebral lymphatic vessels, most studies to date adopt inversion recovery based sequences such as fluid-attenuation inversion recovery (FLAIR) and black blood MRI (5,41), or fast gradient-echo (GRE) sequences (19-23,30-34). These existing approaches typically take at least a few minutes to achieve whole brain coverage and sufficient spatial resolution, which provides a relatively low temporal resolution. Moreover, few studies have performed a systemic investigation to optimize the contrast for the detection of Gd-based signal changes in the CSF, which can be affected by the choice of a number of imaging parameters and also depends on the concentration of Gd. Therefore, the purpose of the current study is to develop an MRI sequence which can fulfill the following criteria in order to image Gd-based signal changes in the CSF:

1. It should effectively suppress signals from gray matter (GM), white matter (WM), and most importantly blood in the brain. This is because blood vessels have similar dimension and often run closely along cerebral lymphatic vessels in the brain (3-5);
2. It should offer sufficient MR signal contrast in the CSF before and after Gd administration;
3. It should minimize the extravascular effects from the Gd contrast. It is well-known that the magnetic susceptibility effects induced by the Gd contrast can alter MR signals within the vessels (intravascular effects) as well as in the adjacent regions (extravascular effects) (38,39). The extravascular effect is a main confounder for the spatial specificity of Gd-based MR signal changes. This is particularly important as the CSF space can be quite small at many locations and is often in the close vicinity of small blood vessels in the brain;
4. It should have a high temporal resolution (time of repetition or TR < 10s), a fine spatial resolution (1-0.65mm isotropic voxel) and whole brain coverage.

To realize the above requirements, we propose to use a turbo spin echo (TSE, also known as fast spin echo or FSE) sequence with optimized parameters and advanced fast imaging techniques. Here, we demonstrate the theoretical calculations, phantom validations and initial results in healthy human subjects with this proposed MRI approach for dynamic susceptibility contrast in the CSF (cDSC) . Note that the development of this methodology does not rely on any particular theory on CSF circulation in human brains. The focus of this study is to develop and optimize MRI pulse sequences for the measurement of Gd distribution in the CSF space.

3.2 Methods

3.2.1 MRI pulse sequence design

A three-dimensional (3D) TSE sequence from the standard clinical protocols provided by the vender was adopted. The following modifications were implemented based on this sequence according to the four requirements described above:

1. Because CSF T2 is much longer than that of GM, WM and blood in the brain (**Table 2**), long echo time (TE>600ms) (65,66) was used to minimize signals from GM, WM and blood, and separate the CSF signal from the rest of the brain.
2. The following equation can be derived for MR signal contrast (ΔS) in the CSF with (S_{Gd}) and without Gd (S_0) in a 3D TSE sequence:

$$\Delta S = S_{Gd} - S_0 = \left(1 - e^{-\frac{TR}{T1_{Gd}}}\right) \times e^{-\frac{TE}{T2_{Gd}}} - \left(1 - e^{-\frac{TR}{T1_0}}\right) \times e^{-\frac{TE}{T2_0}},, \qquad [1]$$

where TE is the effective echo time (67), $T1_{Gd}$ and $T1_0$ are T1 relaxation times of CSF with and without Gd, and $T2_{Gd}$ and $T2_0$ are T2 relaxation times of CSF with and without Gd. The complete derivation is shown in the **Appendix A**. Note that Eq. [1] describes the gross MR signal acquired at the center of k-space (k0), which is shown here to illustrate the basic principle of the proposed approach. In the simulations (see next section), however, stepwise MR signal evolution during the entire 3D TSE echo train was calculated using the Bloch equations instead of Eq. [1]. Gd shortens both T1 and T2 in the CSF, which affects the TSE signal oppositely. Therefore, two types of sequences were evaluated: T1-dominant sequences that furnishes a positive contrast (increased signal after Gd injection) and T2-dominat sequences that furnishes a negative contrast (decreased signal after Gd injection) in the CSF. When the field of view (FOV) and voxel

size were set, the following parameters were adjusted to realize optimal contrast: the number of shots in the 3D TSE readout, TR, and TE. Note that these parameters can interplay with each other in many ways. For instance, the shortest TR and TE can change with different numbers of shots. We will show the optimization process in the Simulation section.

3. To avoid the extravascular effects from Gd, a spin echo (SE) based sequence was adopted, which is known to have dominant intravascular but minimal extravascular effects (38,68) compared to commonly used GRE based sequences.
4. To get whole brain coverage with a temporal resolution of <10s and a sub-millimeter spatial resolution, the Compressed-Sensing SENSE (CS-SENSE) technique (47,69) was used to significantly accelerate the acquisition.

3.2.2 Theoretical simulation and optimization

Bloch simulations (instead of the analytical form in Eq. [1]) were performed to calculate the MR signal evolution during the 3D TSE readout, and compare signals in different types of brain tissues before and after Gd injection. In-house code programmed in Matlab (MathWorks, Natick, MA, USA) were used for the simulations. **Table 2** summarizes the literature values for the parameters used in the simulations (references in the table captions). The relaxation times of CSF after Gd injection were calculated based on the relaxivity values r1 and r2 for the Gd contrast medium Prohance (or Gadoteridol; Bracco S.p.A., Milan, Italy; 0.5 mmol/ml) used in this study with a standard dosage of 0.1 mmol/kg. The concentration of Gd in blood was assumed to be 1 mmol/L for a typical healthy human subject (estimated from the Gd dosage, a body weight of 100kg and a total blood volume of 5L). The concentration of Gd in CSF was assumed to be 0.2 mmol/L, one

fifth of that in blood (a rough estimate due to lack of literature, which will be measured with the proposed method in this study). A second simulation was performed with varying Gd concentrations in CSF to investigate its effects on the MR signals. The goal of the simulations is to find an optimal sequence with minimal blood signal and sufficient contrast for CSF before and after Gd injection.

Table 2: Literature values for key parameters used in the simulations

	CSF	CSF with Gd	Blood	Blood with Gd	GM	WM
3T						
T1 (ms)	4310 (70)	1262 [c]	1649 (71)	199 [c]	1607 (72)	838 (72)
T2 (ms)	1400 (73)	717 [c]	120 [d] (74)	72 [c]	63 (75)	77 (75)
r1 (L/mmol/s) [a]		2.8 (76)		4.4 (76)		
r2 (L/mmol/s) [b]		3.4 (76)		5.5 (76)		
7T						
T1 (ms)	4425 (70)	1272 [c]	2089 (71)	205 [c]	1939 (72)	1126 (72)
T2 (ms)	1000 (73)	595 [c]	80 [d] (77)	56 [c]	39 (75)	50 (75)
r1 (L/mmol/s) [a]		2.8 (76)		4.4 (76)		
r2 (L/mmol/s) [b]		3.4 (76)		5.5 (76)		

[a] r1 = T1 relaxivity of gadolinium contrast in a certain medium (CSF or blood). It is not field dependent, but changes with the medium;

[b] r2 = T2 relaxivity of gadolinium contrast in a certain medium (CSF or blood). It is not field dependent, but changes with the medium;

[c] Defined in Eqs. [S2] and [S3].

[d] In the proposed approach, we aim to suppress the blood signal using long echo time (TE). Therefore the longest blood T2 values (fully oxygenated blood) were used in the simulations.

3.2.3 Simulation validation with MRI phantom scans

Phantom scans were performed using the proposed approach: 1) to validate the simulation results; 2) to evaluate the contrasts with different concentrations of Gd in the CSF. Four plastic tubes (length=12cm, diameter=30mm) were filled with solutions of water and Gd of four different concentration levels, respectively, to produce similar T1 and T2 values of CSF with Gd (0, 0.1, 0.5, and 1 mmol/l). The phantoms were scanned with the following MRI sequences on both 3T and 7T: 1) inversion recovery TSE sequences to determine T1 values: TR/TE=30000/40ms, 17 times of inversion (TI) from 100ms to 3300ms with a step of 200ms; 2) a multi-echo TSE sequence to determine T2 values: TR=30000ms, 30 TEs from 58ms to 3248ms with a step of 110ms, voxel =2×2×5mm^3; 3) the proposed 3D TSE sequence with various combinations of imaging parameters in the simulations; and 4) 3D TSE with a long TR=30000ms to measure the equilibrium signal M0 for signal normalization.

3.2.4 Human cDSC MRI scans

Ten healthy volunteers were recruited for this study (3T: four female and four male, age 23-63 years, 42.5±16.5 years; 7T: one female and one male, both age 28 years). All

participants were screened with a creatinine measurement of less than 1.4 mg/dl on whole blood to be eligible for an MRI scan with Gd. This study was approved by the Johns Hopkins Institutional Review Board, and written informed consent was obtained from each participant. The parameters for the proposed 3D TSE scan were chosen based on the simulations and phantom studies.

The following scans were performed on 3T for each subject sequentially: 1) a time-of-flight (TOF) MR angiography (MRA) scan to facilitate the identification of arterial vessels: voxel = 0.4×0.6×1.3mm^3, 200 slices, TR/TE = 22/3.5ms, scan duration = 6min21s; 2) a susceptibility-weighted-imaging (SWI) scan to facilitate the identification of venous vessels: voxel = 1mm isotropic, 130 slices, TR=51ms, 6 TEs from 10ms to 45ms with a step of 7ms, scan duration = 6min49s; 3) 3D FLAIR: TR/TI/TE = 4800/1650/307ms, TSE factor =167, CS-SENSE = 8.5, voxel = 1mm isotropic, 130 slices, scan duration = 2min10s; 4) dynamic 3D TSE (the following parameters were chosen based on the simulation and phantom results, please see *Healthy human subject results* in the Results section): TR/TE/echo spacing (ES) = 9000/1289/4.4ms, TSE factor = 950, number of shots = 1, partial Fourier = 0.75×0.7, CS-SENSE = 12, voxel = 0.75mm isotropic, 173 slices, and the sequence was performed continuously while 33 and 107 volumes of whole brain images were acquired immediately before and after Gd injection, respectively, total scan duration = 21 minutes, head specific absorption rate (SAR)<15% of the FDA limit; 5) a second FLAIR scan (post-Gd injection) with identical parameters as the first FLAIR scan.

The following scans were performed on 7T for each subject sequentially: 1) 3D magnetization-prepared rapid acquisition gradient-echo (MPRAGE): TR/TI/TE = 4.0/1000/1.8ms, SENSE = 2×2, voxel = 1mm isotropic, 180 slices, scan duration = 2min15s; 2) dynamic 3D TSE: TR/TE/ES = 9000/1187/4.7ms, TSE factor = 950, number

of shots = 1, voxel = 0.75mm isotropic, partial Fourier = 0.7×0.7, SENSE = 3×1, 40 slices, and the sequence was performed continuously while 20 and 80 volumes of whole brain images were acquired immediately before and after Gd injection, respectively, total scan duration = 15 minutes, head SAR<15% of the FDA limit; 3) a second MPRAGE scan (post-Gd injection) with identical parameters as the first MPRAGE. Note that because the compressed SENSE technique was not available on our 7T system when this study was conducted (more in Discussions), partial brain coverage around the dural sinuses was acquired on 7T in this study. Besides, an MPRAGE scan (instead of FLAIR) was acquired pre- and post-Gd injection for anatomical reference on 7T.

3.2.5 Data analysis

The statistical parametric mapping (SPM) software package (Version 12, Wellcome Trust Centre for Neuroimaging, London, United Kingdom; http://www.fil.ion.ucl.ac.uk/spm/) and other in-house code programmed in Matlab (MathWorks, Natick, MA, USA) were used for image analysis. The 3D TSE images acquired before and after Gd injection were motion corrected using the realignment routine in SPM. Other images were co-registered to the 3D TSE images. Regions of interest (ROI) were manually delineated on the anatomical images for each subject, which were then overlaid onto all MRI scans from the same subject for further analysis. Three ROIs where cerebral lymphatic vessels have been identified in human brains were chosen, including regions around the dural sinuses, middle meningeal artery, and cribriform plate (3-5). The ROI around the dural sinuses covers the previously reported cerebral lymphatic vessels running alongside the superior sagittal sinus (3-5), which can be appreciated as vessels lateral to the superior sagittal sinus between the periosteal dura mater and meningeal dura

mater in a coronal view on FLAIR and MPRAGE images. The ROI around branches of the middle meningeal artery and branches of the extracranial carotid artery was identified mainly from the co-registered MRA images by tracing the branches of bilateral middle meningeal arteries on the dura mater starting from the foramina spinosa on the skull. The ROI around the cribriform plate covered the area between the cribriform and the dura matter adjacent to the olfactory bulb and olfactory tract in the anterior cranial fossae identified on FLAIR and MPRAGE images. The ROI selection was performed by two experienced neuroradiologists (N.K. and J.J.P.). The relative signal change ($\Delta S/S$) was calculated as the difference signal between pre- and post-Gd periods divided by average pre-Gd signal (Eq. [S5]). Temporal signal-to-noise ratio (tSNR) was taken as the signal divided by standard deviation along the time course in each voxel. Contrast-to-noise ratio (CNR) was defined as the product of tSNR and $\Delta S/S$. A threshold of CNR>1 was applied in all 3D TSE scans to exclude voxels with high noise levels. Onset time (T_{onset}) was defined as the time when significant signal change is detected in the dynamic 3D TSE scans after Gd injection. Peak time (T_{peak}) was defined as the time when maximum signal change is detected in the dynamic 3D TSE scans after Gd injection. The concentration of Gd in the CSF ([Gd]) was estimated from the 3D TSE signals based on the same Bloch equations used in the 3D TSE simulations. Two-sample two-tailed t-tests with unequal variances were used for statistical analysis.

3.3 Results

3.3.1 Optimization of MRI pulse sequence parameters optimization with Bloch simulation

In the proposed 3D TSE sequence, three key parameters can be adjusted to maximize the signal contrast in CSF before and after Gd injection: shot number, TR, and TE. Note that there parameters are not independent and can interplay with each other. All possible combinations of these parameters were investigated using Bloch simulations, but only selected combinations were demonstrated here to illustrate the optimization process. Graphs with 2D curves were presented instead of 3D surface plots for the ease of visualization of the main results.

Figures 8(a-c) show the main simulation results for T1-dominant 3D TSE sequences (positive contrast, increased CSF signal with Gd) with different choices of shot number. Fractional MR signals (Mz/M0) were plotted as functions of volume TR. Here, TE was fixed at the shortest value determined by the readout train (linear phase encoding profile), as longer TE will further reduce CSF signals with little improvement for the contrast in CSF with and without Gd in the T1-dominant sequence. Note that the shortest TE decreases with shot number. The simulations show that the TE is sufficiently long to suppress GM, WM and pre-Gd blood signals. After Gd injection, the CSF signal increases. The contrasts in CSF signals before and after Gd injection peak at relatively short TRs for a given shot number, and the maximum contrast increases with shot number. **Appendix A Table S1a** demonstrates the tradeoff between maximum CSF Gd contrast and temporal resolution (volume TR) with various shot numbers. In general, higher Gd contrast in the CSF can be achieved at the cost of lower temporal resolution. Note that the post-Gd blood

signals also increase with larger shot numbers (and thus shorter TE), and was significantly positive when TE was too short (**Figures 8c**), which should be avoided for our purpose.

Figures 8(d-f) show the main simulation results for T2-dominant 3D TSE sequences (negative contrast, decreased CSF signal with Gd). Here, as long TR is preferred for T2-weighting, only single shot results were shown. Simulations with three different volume TR choices were presented, as the longer interval between each image volume provides extra time for longitudinal relaxation and thus increases the overall MR signal. Fractional MR signals (Mz/M0) were plotted as functions of TE. As shown in respective curves, signals in GM, WM and blood without Gd are all sufficiently suppressed in all three TRs for TE longer than approximately 600ms. After Gd injection, the CSF signal decreases. The contrasts in CSF signals before and after Gd injection peak at long TEs, and the maximum contrast increases with TR. **Appendix A Table S1b** demonstrates the tradeoff between maximum Gd contrast and temporal resolution (volume TR). Similar to the T1-dominant sequences, higher Gd contrast in the CSF can be achieved at the cost of lower temporal resolution. Note that the post-Gd blood signal is still sufficiently suppressed in the T2-dominant sequences (**Figures 8(d-f)**).

Simulation results at 7T are shown in **Figures 8(g-l)** and **Appendix A Tables S1c,d**. Similar to the 3T results, the GM, WM and blood signals are suppressed for TE longer than approximately 500ms , and the maximum contrast in CSF before and after Gd injection increases with volume TR. Note that since the simulations were performed using slightly different imaging parameters on 3T and 7T, mainly due to the different parallel imaging methods that are currently available on the scanners (CS-SENSE on 3T, and SENSE on 7T), a direct comparison between 3T and 7T is not possible in this study.

However, we will discuss the field dependence of the proposed approaches in Discussions.

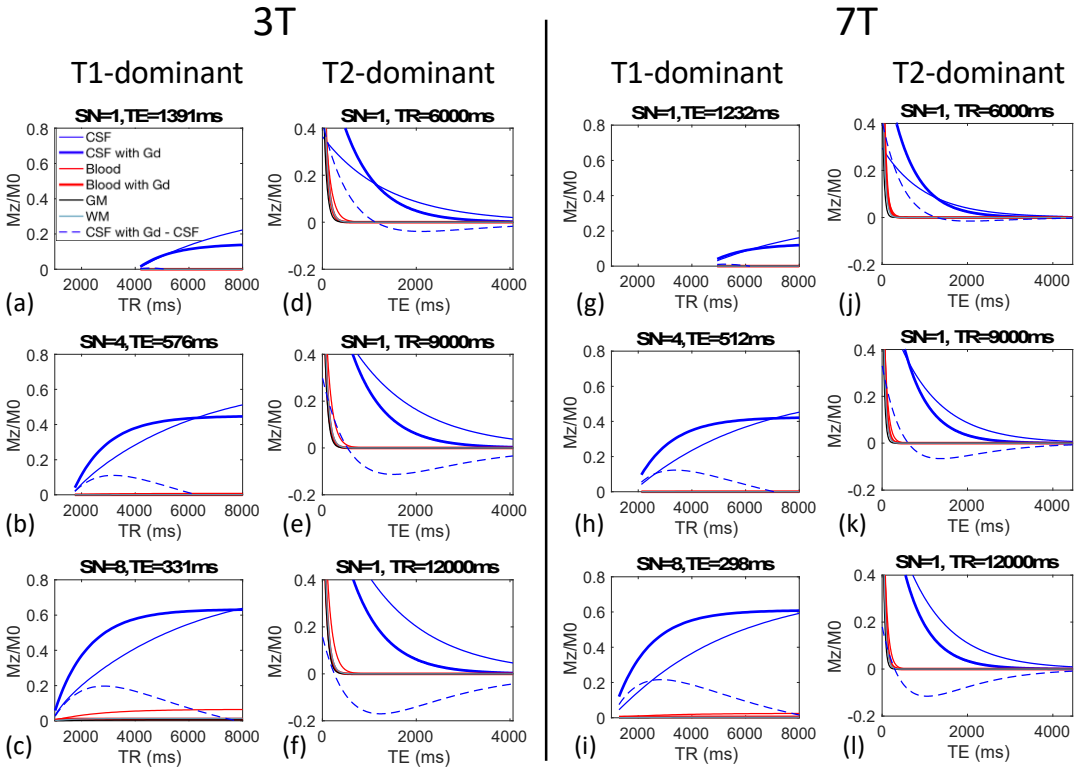

Figure 8: Simulation results for the 3D TSE sequences: (a-c) 3T, T1-dominant; (d-f) 3T, T2-dominant; (g-i) 7T, T1-dominant; (j-l) 7T, T2-dominant. The fractional MR signals (Mz/M0) are displayed as functions of shot number (SN), TE and TR. Signals of gray matter (GM), white matter (WM) and blood are most suppressed (lines close to zero). The contrast is defined as ("CSF with Gd" – CSF).

In all simulations above, the concentration of Gd in the CSF was assumed to be one fifth of that in blood (**Table 2**), based on the fact that with i.v. injection, the Gd contrast leaks out from the dural blood vessels which lacks a BBB into the CSF (15-18). However, this is a very rough estimation, and Gd concentration is known to be a key factor that can have dramatic effects on MR signals (44). **Figure 9** shows simulation results for the relationship between the maximum contrast in the CSF with and without Gd and the

concentration of Gd in CSF. The T1-dominant sequences show a biphasic relationship with Gd concentration. For instance, in **Figure 9b**, the positive contrast in CSF increases with Gd concentration initially, peaks at [Gd] = 0.22 mmol/L, decreases for [Gd] > 0.22 mmol/L, and becomes negative for [Gd] > 0.61 mmol/L. This can be problematic for data interpretation when the *in vivo* Gd concentration in CSF is uncertain. In the T2-dominat sequence, the contrast in CSF is always negative, increases (more negative) monotonically with Gd concentration, and plateaus for approximately [Gd] > 0.5 mmol/L.

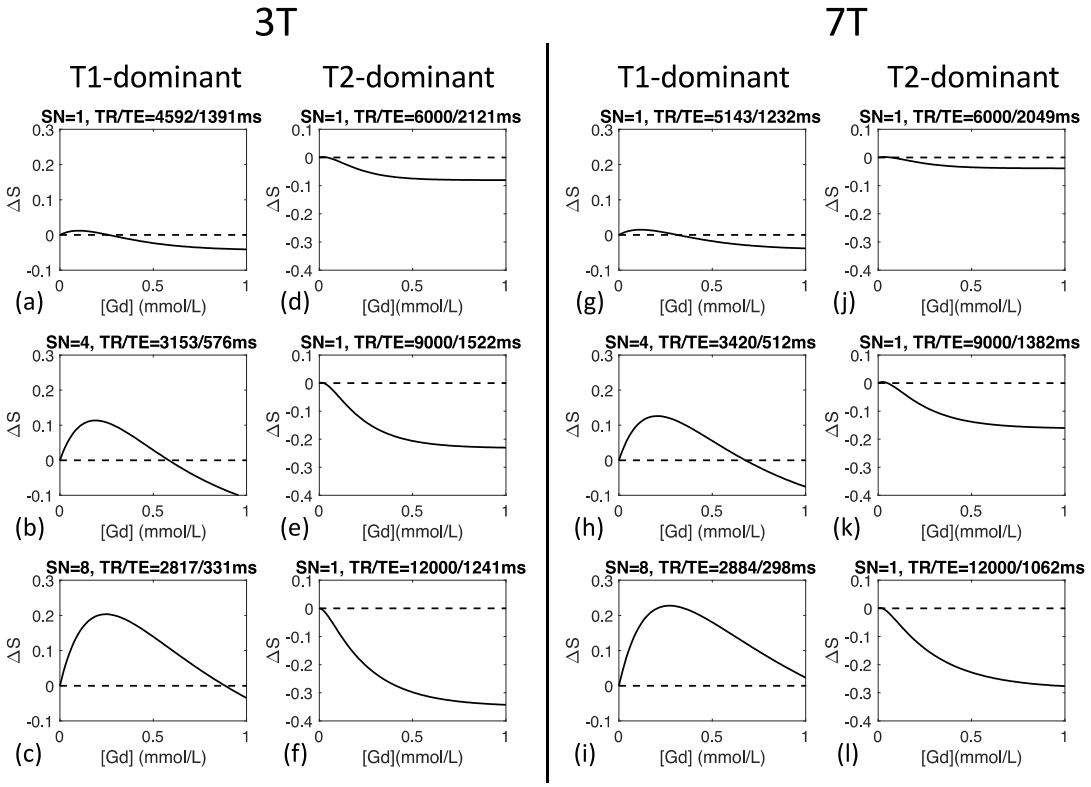

Figure 9: Simulations of the signal contrast with and without Gd in CSFas a function of Gd Concentration ([Gd]). The parameters (shot number (SN), TR and TE) that correspond to maximum contrast in each sequence (Figure 1 and Table 2) were used here. (a-c) 3T, T1-dominant; (d-f) 3T, T2-dominant; (g-i) 7T, T1-dominant; (j-l) 7T, T2-dominant. The fractional MR signals (Mz/M0) are displayed as functions of Gd Concentration ([Gd]). In T1-dominant 3D TSE, the positive contrast shows a biphasic relationship with Gd concentration. In T2-dominant 3D

TSE, the negative contrast increases (more negative) monotonically with [Gd] and plateaus for approximately [Gd] > 0.5 mmol/L.

3.3.2 Validation of Bloch simulation results with phantom MRI scans

First, the T1 and T2 values in the constructed tubes were measured at 3T: 0.0mmol/L: T1/T2 = 3215/2103ms, 0.1mmol/L: T1/T2 = 1416/1026ms, 0.5mmol/L: T1/T2 = 503/337ms, 1.0mmol/L: T1/T2 = 378/249ms; and 7T: 0.0mmol/L: T1/T2 = 3325/1798ms, 0.1mmol/L: T1/T2 = 1479/816ms, 0.5mmol/L: T1/T2 = 561/289ms, 1.0mmol/L: T1/T2 = 406/227ms. Second, the phantoms were scanned using selected combinations of imaging parameters optimized from the simulation results. The main purpose here is to validate the simulation results with phantom measures. **Figure 10** demonstrates that the fractional MR signals measured in phantoms agreed well with the corresponding simulation results on both 3T and 7T. The simulation results in **Figure 10** may differ slightly from those in **Figures 8 and 9**, mainly due to the differences in T1 and T2 values measured in these constructed phantoms and the literature values used previously. The phantom results also confirmed the effects from Gd concentration simulated in **Figure 8**.

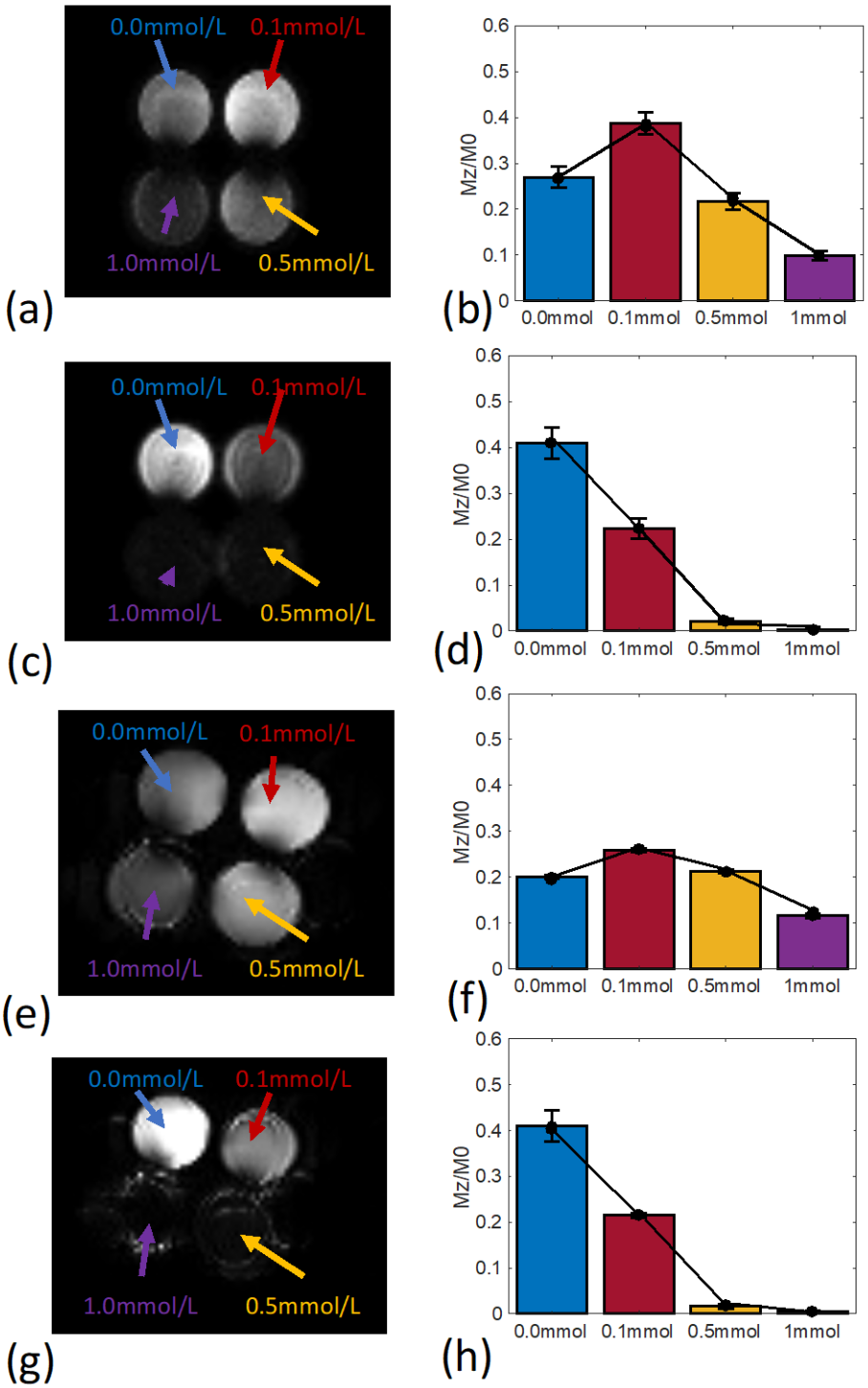
0.0mmol/L
0.1mmol/L
1.0mmol/L
0.5mmol/L
(a)
(b)
Mz/M0
0.0mmol
0.1mmol
0.5mmol
1mmol
(c)
(d)
(e)
(f)
(g)
(h)

Figure 10: Phantom results to validate simulations. MR images of the phantoms, fractional MR signals averaged over the entire volume (Mz/M0) in each tube (bars), and the corresponding simulation results (curves) are shown for: (a,b) 3T, T1-dominant sequence, TR/TE = 2500/482ms, shot number (SN) = 5; (c,d): 3T, T2-dominant, TR/TE = 9000/1391ms, SN = 1; (e,f): 7T, T1-dominant, TR/TE = 2000/394ms, SN = 6; (g,h): 7T, T2-dominant, TR/TE = 9000/1232ms, SN=1.

3.3.3 Determination of MRI parameters for human scans

Based on the simulations and phantom results, the T2-dominant 3D TSE sequence was chosen for subsequent human scans. As shown in **Figure 8**, the post-Gd blood signal can be insufficiently suppressed in T1-dominant sequences. More importantly, the contrast in CSF with and without Gd increases monotonically with Gd concentration in T2-dominant sequences. Therefore, the results will not be confounded when the *in vivo* Gd concentration is uncertain. Furthermore, it provides a potential method to estimate Gd concentration *in vivo*. A temporal resolution (volume TR) of 9s was chosen for the human scans in the current study. Since little literature is available on the time scale of dynamic signal change in CSF after i.v. injection of Gd, a medium TR was chosen to balance the tradeoff between temporal resolution and maximum contrast. The results from this study will be used to guide future studies for the choice of TR.

3.3.4 Gd induced dynamic signal changes captured by cDSC MRI

Figures 11-13 show typical 3T results from one participant in the three ROIs described in Methods, where cerebral lymphatic vessels have been identified in human brains, including regions around the dural sinuses, middle meningeal artery, and cribriform plate (3-5). In all three regions, CSF signal changes after Gd injection were detected in FLAIR and the proposed 3D TSE sequence. With a temporal resolution of 9s, the 3D TSE

sequence was able to detect dynamic signal changes in these regions, from which several parameters including T_{onset}, T_{peak}, ΔS/S and [Gd] can be estimated. Maps of these parameters in this participant are shown for each ROI. **Table 3** shows average parameter values from all participants in the three regions. The concentration of Gd in CSF in these three regions was approximately 0.2 mmol/L, one fifth of that in blood after i.v. Gd injection in healthy human subjects. This is also the assumed Gd concentration in CSF (0.2 mmol/L) in all simulations in this study. The CSF signal decrease after Gd injection detected in 3D TSE preserved for the entire acquisition period (approximately 16 minutes after Gd injection).

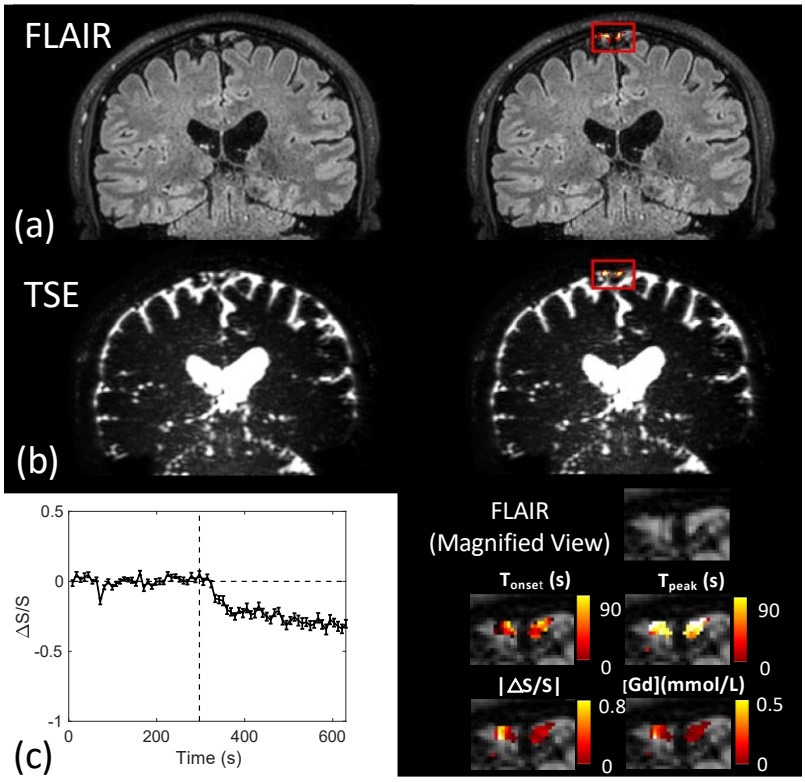

Figure 11: Human cDSC MRI images in the Dural sinuses (DS) region. Representative results from human scans using the optimized T2-dominant 3D TSE sequence on 3T (from one subject, 51 years old, male). Results from the

manually drawn region-of-interest (ROI, red boxes) around the dural sinuses (DS) (especially the superior sagittal sinus) are shown. The ROI selection was performed by two experienced neuroradiologists (N.K. and J.J.P.). (a) The 3D FLAIR image similar to FLAIR used in previous reports (5) is shown on the left. Relative signal changes (ΔS/S) detected with the 3D FLAIR sequence in the ROI overlaid on the corresponding FLAIR image is shown on the right. (b) The image acquired with the proposed 3D TSE sequence is shown on the left. Relative signal changes (ΔS/S) detected with 3D TSE in the ROI overlaid on the corresponding 3D TSE image is shown on the right. Only voxels with a contrast-to-noise ratio (CNR) > 1 were highlighted in the image (see Data analysis). (c) The average time course detected using the optimized T2-dominant 3D TSE sequence from the ROI is shown on the left. Only voxels with CNR > 1 were included. The error bars indicate standard deviations. The vertical dashed lines indicate the time when Gd is injected. The right panel shows a magnified view of the FLAIR image in the ROI, and four maps of the following parameters extracted from the dynamic time courses detected in 3D TSE overlaid on the FLAIR image: T_{onset} = onset time, T_{peak} = time to peak, absolute value of relative signal change |ΔS/S| between pre- and post-Gd, [Gd] = concentration of Gd. The color bars indicate the corresponding scales of each parameter.

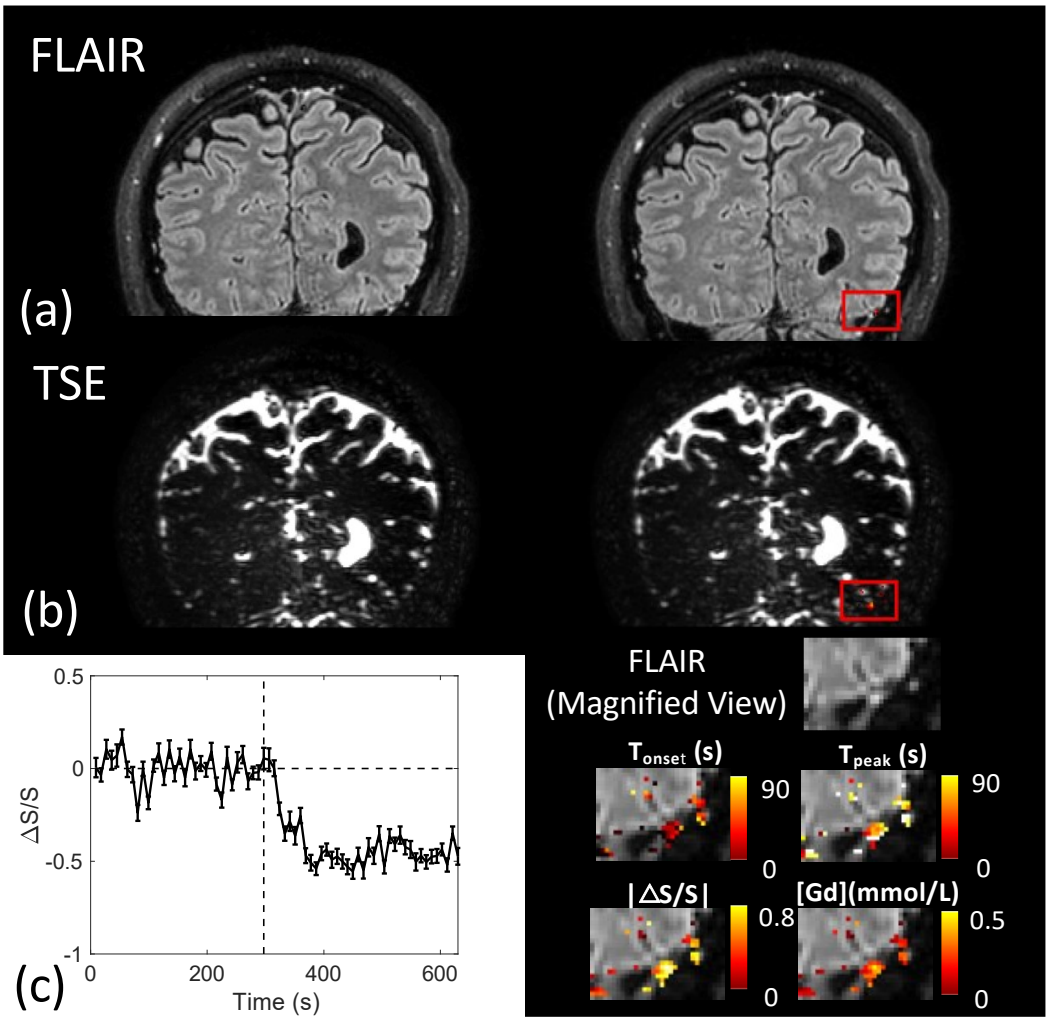

Figure 12: Human cDSC MRI images in the Middle meningeal artery (MA) region. Representative results from human scans using the optimized T2-dominant 3D TSE sequence on 3T (from one subject, 51 years old, male). Results from the manually drawn region-of-interest (ROI, red boxes) around branches of the middle meningeal artery (MA) and branches of the extracranial carotid artery are shown. The ROI selection was performed by two experienced neuroradiologists (N.K. and J.J.P.). (a) The 3D FLAIR image similar to FLAIR used in previous reports (5) is shown on the left. Relative signal changes (ΔS/S) detected with the 3D FLAIR sequence in the ROI overlaid on the corresponding FLAIR image is shown on the right. (b) The image acquired with the proposed 3D TSE sequence is shown on the left. Relative signal changes (ΔS/S) detected with 3D TSE in the ROI overlaid on the corresponding 3D TSE image is shown on the right. Only voxels with a contrast-to-noise ratio (CNR) > 1 were highlighted in the image (see Data analysis). (c) The average time course detected using the optimized T2-dominant 3D TSE sequence from the ROI is shown on the left. Only

voxels with CNR > 1 were included. The error bars indicate standard deviations. The vertical dashed lines indicate the time when Gd is injected. The right panel shows a magnified view of the FLAIR image in the ROI, and four maps of the following parameters extracted from the dynamic time courses detected in 3D TSE overlaid on the FLAIR image: T_{onset} = onset time, T_{peak} = time to peak, absolute value of relative signal change |ΔS/S| between pre- and post-Gd, [Gd] = concentration of Gd. The color bars indicate the corresponding scales of each parameter.

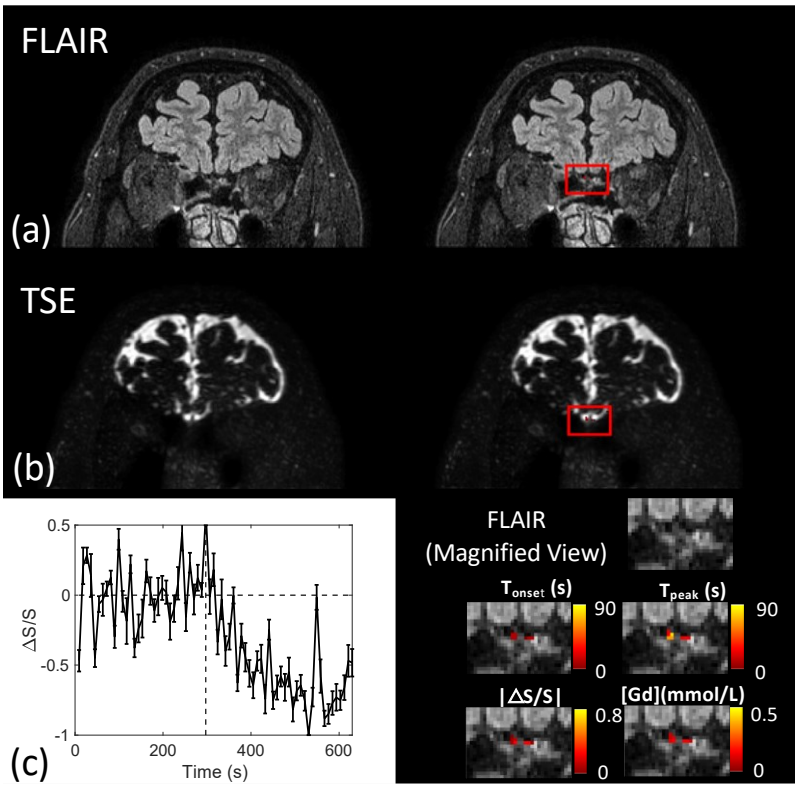

Figure 13: Human cDSC MRI images in the Cribriform plate (CP) region. Representative results from human scans using the optimized T2-dominant 3D TSE sequence on 3T (from one subject, 51 years old, male). Results from the manually drawn region-of-interest (ROI, red boxes) around the cribriform plate (CP) are shown. The ROI selection was performed by two experienced neuroradiologists (N.K. and J.J.P.). (a) The 3D FLAIR image similar to FLAIR used in previous reports (5) is shown on the left. Relative signal changes (ΔS/S) detected with the 3D FLAIR sequence in the ROI overlaid on the corresponding FLAIR image is shown on the right. (b) The image acquired with the proposed 3D TSE sequence is shown on the left. Relative signal changes (ΔS/S) detected with 3D TSE in the ROI overlaid on the corresponding 3D TSE image is shown on the right. Only voxels with a contrast-to-noise ratio (CNR) > 1 were highlighted in the

image (see Data analysis). In the proposed long TE 3D TSE sequence, hyperintensities correspond to CSF regions while the cribriform plate (bone structure) should be dark. The images show that the highlighted voxels are within a continuous CSF region extending from the cerebrum just below the gyrus rectus bilaterally, and above the darker cribriform plate below the bright CSF region. (c) The average time course detected using the optimized T2-dominant 3D TSE sequence from the ROI is shown on the left. Only voxels with CNR > 1 were included. The error bars indicate standard deviations. The vertical dashed lines indicate the time when Gd is injected. The right panel shows a magnified view of the FLAIR image in the ROI, and four maps of the following parameters extracted from the dynamic time courses detected in 3D TSE overlaid on the FLAIR image: T_{onset} = onset time, T_{peak} = time to peak, absolute value of relative signal change |ΔS/S| between pre- and post-Gd, [Gd] = concentration of Gd. The color bars indicate the corresponding scales of each parameter.

Figure 14 shows typical 7T results from one participant. Because of the partial brain coverage (see Methods), only the results in the dual sinus region was shown. Signal changes after Gd injection were detected in MPRAGE (**Figure 14a**) and 3D TSE (**Figure 14b**). Note that similar to previous reports (5), MPRAGE images showed Gd induced signal changes in both blood and CSF. Dynamic signal changes was detected with 3D TSE with a temporal resolution of 9s (**Figure 14c**). Several parameters (T_{onset}, T_{peak}, ΔS/S and [Gd]) were calculated from the dynamics signal changes and their maps were shown in **Figure 14c**.

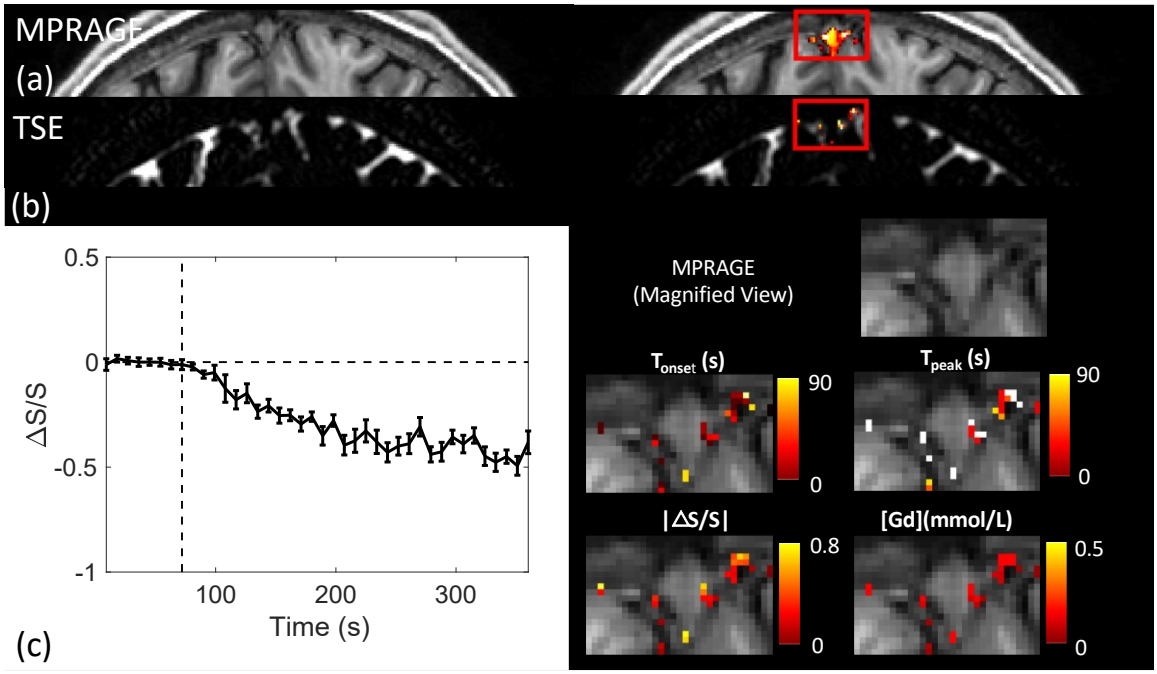

Figure 14: Human cDSC MRI images acquired on 7T. Representative results from human scans using the optimized T2-dominant 3D TSE sequence on 7T (from one subject, 28 years old, male). Note that because the CS-SENSE technique was not available on our 7T system when this study was conducted (more in Discussions), partial brain coverage around the dural sinuses was acquired on 7T in this study. Images from the region-of-interest (ROI, red boxes) around the dural sinuses (DS) are shown. The ROI selection was performed by two experienced neuroradiologists (N.K. and J.J.P.). (a) The 3D MPRAGE image similar to MPRAGE used in previous reports (5) is shown on the left. Relative signal changes (ΔS/S) detected with the 3D MPRAGE sequence in the ROI overlaid on the corresponding MPRAGE image is shown on the right. Note that similar to previous reports (5), MPRAGE images showed Gd induced signal changes in both blood and CSF. (b) The image acquired with the proposed 3D TSE sequence is shown on the left. Relative signal changes (ΔS/S) detected with 3D TSE in the ROI overlaid on the corresponding 3D TSE image is shown on the right. Only voxels with a contrast-to-noise ratio (CNR) > 1 were highlighted in the image (see Data analysis). (c) The average time course detected using the optimized T2-dominant 3D TSE sequence from the ROI is shown on the left. Only voxels with CNR > 1 were included. The error bars indicate standard deviations. The vertical dashed lines indicate the time when Gd is injected. The right panel shows a magnified view of the MPRAGE image in the ROI, and four maps of the following parameters extracted from the dynamic time courses detected in 3D TSE overlaid on the MPRAGE image: T_{onset} = onset time, T_{peak} = time to peak, absolute value of relative signal change |ΔS/S| between pre- and post-Gd, [Gd] = concentration of Gd. The color bars indicate the corresponding scales of each parameter.

Table 3 shows average parameter values from all participants scanned at 7T, which were comparable to corresponding results at 3T (P=0.95 for T_{onset}, P=0.70 for T_{peak}, and P=0.13 for ΔS/S and [Gd]). The CSF signal decrease after Gd injection detected in 3D TSE preserved for the entire acquisition period (approximately 12 minutes after Gd injection).

Table 3: Quantitative results from human scans at 3T (n = 8) and 7T (n = 2)

	3T			7T
	DS	**MA**	**CP**	**DS**
T_{onset} (s)	**18.3 ± 8.8**	**12.1 ± 7.7**	**28.7 ± 23.8**	**18.1 ± 8.1**
T_{peak} (s)	**52.7 ± 22.4**	**42.4 ± 21.7**	**71.8 ± 32.9**	**57.2 ± 23.6**
ΔS/S (fractional)	**-0.28 ± 0.06**	**-0.33 ± 0.08**	**-0.46 ± 0.18**	**-0.33 ± 0.02**
[Gd] (mmol/L)	**0.16 ± 0.02**	**0.18 ± 0.02**	**0.24 ± 0.06**	**0.19 ± 0.01**

3.4 Discussion

We demonstrate a 3D TSE sequence with an optimized contrast for the detection of Gd induced MR signal changes in the CSF with a sub-millimeter spatial resolution, a

temporal resolution of <10s and whole-brain coverage. A long TE was used in the sequence so that signals from GM, WM and blood were all suppressed, and only CSF signals can be detected. Therefore, partial volume effects from GM, WM and blood are expected to be minimal, and unlike many existing methods, the spatial resolution (voxel size) in this approach does not need to be smaller than the dimensions of the target structures (the CSF space and the cerebral lymphatic vessels) in order to detect dynamic signal changes in the structures. The main reason for choosing a 3D TSE sequence is that TSE is a pure SE-based sequence that is known to have minimal extravascular effects, which is critical for the spatial specificity of the observed Gd induced MR signals changes in the CSF space. Besides, TSE also has less susceptibility artifacts (geometric distortion and signal dropout) than GRE-based sequences, especially in regions close to tissue/bone and tissue/air boundaries in the brain such as the area around the cribriform plate in which cerebral lymphatic vessels have been visualized (5). Our initial results in healthy human subjects demonstrate that the proposed method can detect dynamic signal changes after Gd injection in the CSF at several locations where cerebral lymphatic vessels have previously been visualized using Gd enhanced FLAIR images (5).

CSF circulation in the human brain has been a topic of investigation for centuries. Recently, several new theories have been proposed in the light of new technologies and discoveries for CSF physiology (78-83). In this study, however, we would like to stress that the technology development of the proposed MRI approach does not rely on any particular theory on CSF circulation in the human brain. Our goal here is to develop and optimize MRI pulse sequences for the measurement of Gd distribution in the CSF space. In fact, the proposed MRI approach can be used to further investigate many proposed theories on CSF circulation in the human brain.

In the current study, the results were demonstrated using Gd contrast administrated via i.v. injection, which is a commonly used procedure for clinical MRI with Gd. Contrast media can also be administrated through other routes, such as intrathecal administration via the spinal canal, or the subarachnoid space, and intracerebroventricular injection (ICVI) through cerebral ventricles as demonstrated in many studies in animals and humans (3,4,6-10,19-32). Compared to i.v. injection, these procedures may have the advantage of allowing the examination of a more complete route of CSF circulation in the brain, although they are more invasive and it usually takes much longer for the Gd contrast to reach the brain region injected from the spinal canal (average arrival time on the order of hours), which may limit its clinical applications. The proposed 3D TSE sequence can also be applied to detect dynamic signal changes in the CSF with these other Gd injection procedures. Our 3D TSE sequence can be optimized with Gd contrasts other than Prohance, or any other exogenous contrast agents with known r1 and r2 values (for choosing proper imaging parameters).

The concentration of Gd can have dramatic effects on MR signals (44). With i.v. injection, the Gd contrast is expected to leak out from the dural blood vessels which lacks a BBB into the CSF (15-18). There is few literature on quantitative measures of Gd concentration in the CSF after i.v. injection. With the proposed approach, the Gd concentration in CSF can be estimated from MR signal changes before and after Gd injection. Our data showed that the Gd concentration in CSF in the three regions investigated were approximately 0.2 mmol/L, which is about one fifth of that in blood after i.v. Gd injection in healthy human subjects. The Gd concentration results were consistent from 3T and 7T. According to Eq. [S8] in the **Appendix A**, when TR is relatively long, the relative signal change in CSF before and after Gd injection ($\Delta S/S$) is only affected by three

parameters: TE, r2, and Gd concentration. As r2 can be measured relatively accurately for given contrast medium (76), the estimation of Gd concentration from ΔS/S in our approach is expected to furnish relatively robust results. One limitation though, is that when the Gd concentration is high (approximately >0.5mmol/L), the CSF contrast before and after Gd injection in T2-dominant 3D TSE sequences.

With the 9s temporal resolution provided by the proposed approach, dynamic signal changes from Gd was measured in three regions where cerebral lymphatic vessels have been identified in human brains, including regions around the dural sinuses, middle meningeal artery, and cribriform plate. There is very little literature on how the Gd distributes in these regions after leaking out from dural blood vessels in both animal and human studies. However, the time to onset (T_{onset}) and time to peak (T_{peak}) of Gd induced signal changes estimated from the measured dynamics time courses were comparable to the timing of signal changes reported in many studies using dynamic contrast enhancement (DCE) MRI in brain tumor patients where Gd often leaks out from the broken BBB in the tumor region (84,85). In all regions analyzed, the CSF signal after Gd injection did not return to baseline (pre-Gd level) for the entire acquisition period in our 3D TSE scans (approximately 12-16 minutes after Gd injection). This can be expected as CSF flow in these regions is expected to be much slower than blood flow, and many human studies have shown Gd based signal changes in the CSF in these regions more than 30 minutes after Gd injection (5) using other MRI methods with lower temporal resolution. The above results from dynamic CSF signal changes were consistent from 3T and 7T. We are currently working to further validate them in animal models.

3.5 Technical considerations

Compared with the inversion recovery based sequences commonly used in previous human studies such as FLAIR and black blood imaging (5,32,33,41), the proposed 3D TSE approach does not have a long inversion recovery period and therefore can achieve higher temporal resolution for tracking dynamic signal changes in the CSF. One can also design an inversion recovery sequence with a very short recovery period (time of inversion, or TI), in which the CSF magnetization is still negative so that the opposite effects from Gd on T1- and T2-dominant signal changes when its magnetization is positive can be combined. However, as T1 effects also contribute to the contrast in such sequences, the maximum contrast in CSF with and without Gd will again show a biphasic relationship with Gd concentration similar to the ones demonstrated in **Figure 9**. Besides, similar contrast can be achieved by the proposed 3D TSE sequences without inversion by simply adjusting TR and TE according to our simulations. As inversion recovery sequences usually require the use of a 180° RF pulse with high power deposition especially at high field, 3D TSE without inversion is preferred. Nevertheless, if the *in vivo* Gd concentration is known, the T1-dominant sequences can still be useful, especially since Gd alters T1 more substantially than T2, which can sometimes (depending on imaging parameters and Gd concentration) lead to stronger contrast in the CSF than T2-dominant 3D TSE.

The simulations are a key step for the optimization of the proposed approach. As described in Methods, it was performed using Bloch equations to calculate the MR signals at each echo in the 3D TSE readout train. The analytical form in Eq. [1] with an effective

TE was only provided to show the basic principles of the MR signal contrast to be optimized in this method, but it was not used in the actual simulations. On the simulated curves for the T2-dominant 3D TSE sequences in **Figures 8(d-f, j-l)**, each data point has two meanings. First, it represents the MR signal at the center of k-space (k0) if this TE were chosen as the effective TE. This is possible because the echoes acquired after the current echo should not affect the signal at the current echo (assuming negligible T1 effects in this long TR T2-weighted sequence). This was used to calculate the maximum contrasts as a function of TE in the simulations (**Appendix A Table S1**). Second, it also shows the MR signal at this phase encoding step during the 3D TSE readout if the entire readout train were performed and the effective TE were chosen at the maximum contrast. As shown in the curves, the signal contrast (before and after Gd) may vary for different echoes and thus for different spatial frequency components in the resulting images. As the T2 of CSF is relatively long compared to T2 of GM and WM, the contrast curves in **Figure 8** showed that >80% of maximum contrast can be achieved for a window of approximately 1300ms around the effective TE in the readout. However, it should be cautioned that the contrast may diminish for higher spatial frequency components in the resulting images outside of this window.

The maximum contrast in CSF signals before and after Gd injection, and therefore the simulations and optimization of the proposed approach, is affected by the T1 and T2 values of CSF. There are some variations in the literature for CSF T1 and T2 values (66), and the relaxation times of lymphatic fluid (LF) in the human body can be slightly shorter that those of CSF (86). According to our simulations, a ±100ms variation in CSF T1 can result in a ±50ms optimal TR in T1-dominant sequences (for maximum contrast shown in **Appendix A Table S1**) and a ±20ms optimal TE in T2-dominant sequences, whereas a

±300ms variation in CSF T2 can result in a ±40ms optimal TR in T1-dominant sequences and a ±150ms optimal TE in T2-dominant sequences. However, as shown in Eq. [S8] in the **Appendix A**, when TR is sufficiently long, variations in T1 and T2 values of CSF have little influence on the relative signal change in CSF before and after Gd injection (ΔS/S). As r2 is largely field independent (76), Eq. [S8] also indicates that ΔS/S in the proposed approach should be largely field independent. Indeed, using the same simulation procedures, it is confirmed that ΔS/S will be identical on 3T and 7T if the same imaging parameters (TR and TE) are used. As the intrinsic signal-to-noise ratio (SNR) in MRI increases with field strength, this approach should still benefit from higher field. At the time when this study was performed, the CS-SENSE parallel imaging technique was not available on our 7T system, which limited the 7T human scans to partial brain coverage. However, CS-SENSE will be installed in the next upgrade on our 7T scanner from the vendor, which should enable the use of whole brain sequences as demonstrated in 3T human scans in this study.

Finally, one limitation in this study is that the current set of MR images (T2, FLAIR, TOF, SWI) are not optimal for identifying bone structures such as the cribriform plate, as this study was originally planned to be primarily a methodological development. Additional scans such as black bone MRI can be added in future studies to better visualize the related structures.

In summary, we demonstrated that dynamic signal changes induced by the distribution of Gd contrast medium in the CSF can be detected in healthy human subjects with an optimized 3D TSE sequence. The concentration of Gd in the CSF can be quantified from the relative signal change in this approach. The proposed methodology does not rely

on any particular theory on CSF circulation in the human brain. We expect it to be a useful tool for human and animal studies on CSF circulation and cerebral lymphatic vessels in the brain using contrast agent based approaches.

Chapter 4

4. Dynamic *dual-spin-echo perfusion (DDSEP) MRI*

4.1 Introduction

The cerebrovascular system and cerebrospinal fluid (CSF) circulation system are two important components in the central nervous system (CNS). While the cerebrovascular system provides blood supply to the brain, CSF circulation is critical for waste clearance from the brain and immune surveillance (87). Recent studies in animals and humans have provided more details regarding CSF transportation and drainage in the CNS (87). First, the glymphatic system has been proposed, which aids CSF and interstitial fluid (ISF) transportation in brain parenchyma from the periarterial space to the perivenous space mainly through the aquaporin-4 (AQP4) membrane protein localized primarily in the end feet of astrocytes (80). Second, cerebral vessels with typical endothelial markers found in lymphatic vessels in other organs have been identified in several parts of the brain. These include the dura matter alongside the dural venous sinuses, regions around the middle meningeal artery and cribriform plate (3-5), areas in the basal part of the skull (6), and several other brain regions in animal models. Some of the meningeal lymphatic vessels have also been visualized in human brain (5). These cerebral lymphatic vessels

may communicate with the glymphatic system and other routes for CSF circulation and are believed to play a crucial role in the drainage of CSF and ISF from brain tissues to cervical lymph nodes (3-6,23,24,26). The study of CSF flow in cerebral lymphatic vessels may provide essential information regarding the clearance of abnormal proteins and metabolites from brain tissues. The methodology developed in the current study is focused on cerebral lymphatic vessels, not the glymphatic system.

Accumulating evidence has indicated the interaction between the microvascular and lymphatic systems in the brain. As the CSF and ISF space in brain parenchyma lie alongside small blood vessels, CSF and ISF in the perivascular space are believed to be primarily driven by the arterial pulsation wave from these small blood vessels (23,24,26). A change in blood flow may lead to impaired lymphatic clearance, both of which may contribute to the pathogenesis of various brain diseases. Therefore, it is of importance to investigate the relationship between the microvascular and lymphatic systems in the brain using *in vivo* imaging methods that can capture the two systems in the same subject. To date, most imaging methods can only measure blood or lymphatic vessels separately. An approach that can measure the two systems in a single scan will offer the advantage of significantly shortened scan time, and more importantly, less confounding effects from physiological variations between scans. For MRI methods based on contrast agents, a combined method will reduce the number of doses of contrast media that need to be administrated in the participants.

Dynamic susceptibility contrast (DSC) MRI is a standard perfusion technique performed routinely in clinical MRI exams (13,14). It can measure several key parameters reflecting the function and integrity of blood vessels, such as cerebral blood flow (CBF) and volume (CBV), and blood brain barrier (BBB) permeability. In typical DSC MRI

experiments, MR images are continuously acquired before, during and after intravenous (IV) administration of Gadolinium (Gd) based contrast agents, generating a response curve from which the microvascular parameters can be derived. Gd-based contrast agents are impermeable to an intact blood-brain barrier (BBB) in cortical blood vessels. Nevertheless, as the dural blood vessels lack such a BBB, the Gd-based contrast agents can cross the dural blood vessel wall and enter the CSF. Therefore, post-contrast MR signal changes can often be observed in the CSF at certain locations within the intra-cranial space (15-18). To date, DSC MRI has been optimized primarily for detecting Gd-induced contrast changes in blood vessels (13). Recently, we developed an MRI approach (40) for the detection of Gd-based signal changes in the CSF, namely DSC MRI in the CSF (cDSC MRI), which can be used to measure perfusion parameters related to cerebral lymphatic vessels in the human brain. Most existing approaches for the measurement of Gd-induced MR signal changes in the CSF and cerebral lymphatic vessels take at least a few minutes to achieve whole brain coverage and sufficient spatial resolution, which provides a relatively low temporal resolution (5,19-23,30-34,41). The cDSC MRI method was optimized to detect dynamic signal changes in the CSF and cerebral lymphatic vessels with a sub-millimeter spatial resolution, a temporal resolution of less than 10 seconds, and whole brain coverage (40).

In the current study, we propose a new MRI approach for concurrent measurement of perfusion parameters related to small blood and lymphatic vessels in the brain within one single scan, termed “dynamic dual-spin-echo perfusion (DDSEP) MRI”. A dual-echo turbo-spin-echo (TSE, also known as fast spin echo or FSE) sequence was optimized for the measurement of Gd-induced blood and CSF signal changes using a short and a long echo time (TE), respectively. In this first proof-of-concept study, the proposed DDSEP MRI

approach was implemented with a multi-slice version, in which 3 slices covering some of the brain regions where cerebral lymphatic vessels have been identified were acquired. Theoretical simulations were performed to optimize the imaging parameters. MRI experiments were performed in healthy human subjects to evaluate the proposed combined approach by comparing it with existing separate methods. Approaches to expand the current sequence to a whole brain scan are discussed based on the results obtained from the current study.

4.2 Methods

4.2.1 MRI pulse sequence design

In order to detect blood and CSF signals in a single MRI scan, MR signals from blood and CSF need to be separated based on their substantially different T1 and T2 values (**Table 2**). In addition, the spatial and temporal resolutions need to be optimized to balance between the two types of measures. Specifically, the sequence design needs to fulfill the following criteria:

1) For blood vessels, a relatively high temporal resolution of 1.5–2.5 s is needed to capture the dynamic changes. A spatial resolution of 2-3 mm is sufficient as in typical DSC MRI scans for measuring blood perfusion parameters. A relatively short TE (~80 ms for spin echo) is considered optimal for blood signals.
2) For CSF in cerebral lymphatic vessels, a relatively low temporal resolution of 5–10s is acceptable, based on the typical onset time measured in previous studies (40). A sub-millimeter spatial resolution is ideal to minimize partial volume effects as cerebral lymphatic vessels often run alongside small blood vessels, although

the voxel size does not need to be smaller than the microvessels if the signals from parenchyma and blood can be effectively suppressed (~0). As CSF T2 is much longer than that of parenchyma and blood in the brain (**Table 2**), a long TE (~ 500 ms) is required to minimize signals from parenchyma and blood.

It should provide sufficient MR signal contrast in blood and CSF before and after Gd administration.

According to these criteria, we propose a dual-echo TSE sequence for simultaneous measurement of blood and CSF signal changes in the brain (**Figure 15**). Similar methods have been used in DSC MRI for measuring dynamic signal changes from blood vessels (13). In our proposed approach, the following unique features were implemented based on the requirements described above:

1) T1-dominant contrast in the CSF: Gd shortens both T1 and T2 values in blood and CSF, which affects the MR signals in the proposed sequence oppositely. In our previous work on cDSC MRI (40), two types of sequences were evaluated for detecting Gd-induced MR signal changes in the CSF. When a relatively short repetition time (TR) is used, the TSE sequence furnishes a T1-dominant positive contrast in CSF after Gd injection. When a relatively long TR is used, the TSE sequence shows a T2-dominant negative contrast in CSF after Gd injection, which was employed in cDSC MRI (40). However, in the proposed combined sequence here, a T1-dominant sequence with short TR was chosen for measuring Gd-induced MR signal changes in both blood and CSF mainly due to the temporal resolution (TR) requirement (see the next point).
2) A temporal resolution of 2 s and a spatial resolution of 1x1x2 mm^3 were chosen to balance the requirements between blood and CSF signals. The temporal

resolution is typical for measuring dynamic changes in blood vessels in DSC MRI and is sufficient for detecting dynamic changes in cerebral lymphatic vessels in human brains based on previous data (40). This is the primary reason for choosing the T1-dominant sequence with short TR in the combined method. Thus, we have a T1-dominant contrast in CSF and a T2-dominant contrast in blood, which has much shorter T1 values than CSF. Note that the spatial resolution here is much finer than the typical spatial resolution of ~2x2x5mm^3 in DSC MRI.

3) A short and a long TE were used in the proposed dual-echo TSE sequence. The first echo (short TE1 = 80 ms) is intended to measure the blood signals similar to DSC MRI. The second echo (long TE2 = 560 ms) measures predominantly the CSF signals with parenchyma and blood signals suppressed.
4) Theoretical simulations (please see the next section) were performed to optimize the imaging parameters in the proposed sequence in order to maximize MR signal contrast in blood and CSF before and after Gd administration.
5) The TSE sequence used is a spin-echo (SE) based sequence, which has better spatial specificity for Gd-induced signal changes (38,68,88,89) compared to the commonly used gradient echo (GRE) based sequences. This is important as cerebral blood and lymphatic vessels are often adjacent to each other (3-5).

4.2.2 Bloch simulation

Bloch simulations were performed to calculate the MR signal and contrast before and after Gd injection from the proposed pulse sequence in blood and CSF. In-house code programmed in Matlab (MathWorks, Natick, MA, USA) was used for the simulations. **Table 2** summarizes the literature values for the parameters used in the simulations. The

relaxation times of CSF after Gd injection were calculated based on the relaxivity values r1 and r2 (**Table 2**) for the Gd contrast medium Prohance (or Gadoteridol; Bracco S.p.A., Milan, Italy; 0.5 mmol/ml) used in this study with a standard dosage of 0.1 mmol/kg. The concentration of Gd in blood was assumed to be 10 mmol/L for the bolus phase typically measured in DSC MRI (13). The concentration of Gd in CSF was assumed to be 0.2 mmol/L, based on the results in healthy human subjects from the literature (40). A second simulation was performed with varying Gd concentrations in blood and CSF to investigate its effects on the MR signals.

4.2.3 Human *DDSEP MRI* scans

MRI scans were performed on a 3 Tesla (3T) Philips human MRI scanner (Philips Healthcare, Best, The Netherlands). A 32-channel phased-array head coil was used for signal reception and a dual-channel body coil for transmit. The Gd contrast agent (Prohance, or Gadoteridol; Bracco S.p.A., Milan, Italy) was administered intravenously (IV) using a standard procedure (dosage=0.1mmol/kg, injection rate=5mL/s).

Eight healthy volunteers were recruited for this study (three female and five male, age 23-36 years, 27±6 years). All participants were screened with a creatinine measurement of less than 1.4 mg/dl on whole blood to be eligible for an MRI scan with Gd. This study was approved by the Johns Hopkins Institutional Review Board, and written informed consent was obtained from each participant. The parameters for the proposed dual-echo TSE scan were chosen based on the simulation results.

The following scans were performed on 3T for each subject sequentially: **1)** a 3D fluid-attenuation inversion recovery (FLAIR) sequence similar to previous cerebral lymphatic vessel studies (5): TR/TI/TE = 4800/1650/307 ms, TSE factor =167,

Compressed-Sensing SENSE (CS-SENSE) = 8.5, voxel = 1mm isotropic, 130 slices, scan duration = 2 minutes and 10 seconds; **2)** a 2D multi-slice FLAIR sequence similar to previous cerebral lymphatic vessel studies (5) but with the same spatial resolution and coverage as the proposed dual-echo TSE sequence in this study: TR/TI/TE = 4800/1650/200ms, TSE factor =41, CS-SENSE = 2, voxel = 1x1x2mm^3, 3 slices, scan duration = 48 seconds; **3)** the proposed dynamic dual-echo TSE sequence (the following parameters were chosen based on the simulation results): TR/TE1/TE2/echo spacing (ES) = 2000/80/560/5.4ms, TSE factor = 120, number of shots = 1, partial Fourier = 0.7, CS-SENSE = 2, voxel = 1x1x2 mm^3, 3 slices, and the sequence was performed continuously while 150 volumes of images were acquired immediately before and after Gd injection, respectively, total scan duration = 10 minutes, head specific absorption rate (SAR) < 15% of the FDA limit; **4)** a second 2D multi-slice FLAIR scan (post-Gd injection) with parameters identical to the first one.

Data acquired using the proposed sequence were compared with data from existing separate sequences: cDSC MRI for lymphatic vessels and standard DSC MRI for blood vessels. Because normally only one standard dose of Gd contrast media is given to a participant during each MRI session, it is not possible to perform all three scans in the same subjects. Therefore, in this study, with the purpose of comparing the three techniques in healthy human subjects, existing data were used for comparison. For the cDSC scan, data from our previous study (40) in eight healthy human subjects (four female and four male, age 23-63 years, 43±17 years) were used. Briefly, for reference, this dynamic 3D TSE cDSC MRI scan was performed with the following parameters: TR/TE/ES = 9000/1289/4.4ms, TSE factor = 950, number of shots = 1, partial Fourier = 0.75×0.7, CS-SENSE = 12, voxel = 0.75mm isotropic, 173 slices, and the sequence was performed

continuously while 33 and 107 volumes of whole brain images were acquired immediately before and after Gd injection, respectively, total scan duration = 21 minutes. In addition, a 3D FLAIR scan was performed before and after Gd injection with the following parameters: TR/TI/TE = 4800/1650/307ms, TSE factor =167, CS-SENSE = 8.5, voxel = 1mm isotropic, 130 slices, scan duration = 2 minutes and 10 seconds. For standard DSC MRI, data from our previous study (90) in eight healthy human subjects (four female and four male, 26 ± 4 years old,) were used. The DSC MRI scan was performed using the following parameters: 2D GRE echo-planar-imaging (EPI), TR/TE = 1000ms/30ms, flip angle = 54°, voxel = 2.8x2.8x5 mm^3, slice gap = 0.5 mm, 18 slices, scan duration = 72 seconds. In addition, a T1-weighted magnetization-prepared rapid acquisition gradient-echo (MPRAGE) was performed with the following parameters: TR/TE/TI = 8.1/3.7/1100 ms, shot interval = 2100 ms, flip angle = 12°, voxel = 1x1x1 mm^3, 160 slices, sagittal slice orientation, and scan duration = 3 minutes and 57 seconds.

Note that the durations of the DDSEP and cDSC scans were chosen to be substantially longer (10-20 minutes) than needed for investigational purposes. Based on the time courses measured in our previous study (40) and the current study, for future clinical applications, the same scans only need to be performed for about 5 minutes to capture the dynamic signal changes before and after Gd administration.

4.2.4 Data analysis

The statistical parametric mapping (SPM) software package (Version 12, Wellcome Trust Centre for Neuroimaging, London, United Kingdom; http://www.fil.ion.ucl.ac.uk/spm/) and other in-house code programmed in Matlab (MathWorks, Natick, MA, USA) were used for image analysis. All dynamic images

acquired before and after Gd injection were motion corrected using the realignment routine in SPM. FLAIR and MPRAGE images were co-registered to the corresponding mean dynamic images after realignment. Masks of cortical grey matter (GM) and white matter (WM) were obtained using the segmentation routine in SPM. Regions of interest (ROI) that cover the cerebral lymphatic vessels were manually delineated on the anatomical (FLAIR or MPRAGE) images for each subject, which were then overlaid onto all MRI scans from the same subject for further analysis. Similar to the data from the proposed DDSEP sequence, the ROIs of cDSC MRI and GRE EPI DSC MRI data acquired in different cohorts of healthy human subjects were identified in the individual space for each participant before subsequent analysis was performed.

The following parameters were computed for all dynamic imaging data. The relative signal change ($\Delta S/S$) was calculated as the difference signal between pre- and post-Gd periods divided by average pre-Gd signal. Temporal signal-to-noise ratio (tSNR) was taken as the signal divided by standard deviation along the time course in each voxel. Contrast-to-noise ratio (CNR) was defined as the product of tSNR and $\Delta S/S$. A threshold of CNR>1 was applied in all dynamic scans to exclude voxels with high noise levels.

The short-TE images in the proposed approach and the standard DSC MRI scans were further analyzed using the Dynamic Susceptibility Contrast MR ANalysis (DSCoMAN) software (https://sites.duke.edu/dblab/dscoman/), from which typical cerebrovascular perfusion parameters such as CBV, CBF, mean transit time (MTT), and time to peak (TTP) were calculated in the entire grey matter region. In addition, in-house Matlab code was used to calculate $\Delta S/S$, onset time (T_{onset}), and return time (T_{return}).

The long-TE images in the proposed approach and cDSC scans were further analyzed using in-house Matlab code, from which $\Delta S/S$, onset time (T_{onset}), TTP, and Gd

concentration ([Gd]) were computed using the same procedure as in our previous study (40). Briefly, onset time (T_{onset}) was defined as the time when significant signal change is detected in the dynamic TSE scans after Gd injection. TTP was defined as the time when maximum signal change is detected in the dynamic TSE scans after Gd injection. Two ROIs where cerebral lymphatic vessels have been identified in human brains were chosen, including regions around the dural sinuses (superior sagittal sinus) and cribriform plate (3-5). The ROI around the dural sinuses covers the previously reported cerebral lymphatic vessels running alongside the superior sagittal sinus (3-5), which can be appreciated as vessels lateral to the superior sagittal sinus between the periosteal dura mater and meningeal dura mater in a coronal view on FLAIR images. The ROI around the cribriform plate covered the area right above the olfactory bulb and olfactory tract identified on FLAIR images. The ROI selection was performed by two experienced investigators (D.C. and J.J.P.).

Two-sample two-tailed t-tests with unequal variances were used for statistical analysis.

4.3 Results

4.3.1 MRI pulse sequence parameters optimization with Bloch simulation

Figures 15(a,b) show the main simulation results for the proposed dual-echo TSE sequence. Fractional MR signals (Mz/M0) and the fractional MR signal changes before and after Gd injection (ΔMz/M0=(Mz_post_Gd-Mz_pre_Gd)/M0) were plotted as functions of TE. In the proposed approach, the pre- versus post-Gd blood contrast ΔMz/M0 (**Figure 15b**) becomes more negative with increasing TE at first, and then gradually returns to zero

at longer TEs. The short TE in the proposed approach was chosen around the maximum pre- versus post-Gd blood contrast ΔMz/M0. The pre- versus post-Gd CSF contrast ΔMz/M0 (**Figure 15b**) shows a positive signal change in this T1-weighted sequence with a TR of 2s, and gradually decreases with increasing TE. The long TE in the proposed approach was chosen when the blood signals (**Figure 15a**) are completely suppressed (~0) in order to minimize the partial volume effects from small blood vessels that often run alongside cerebral lymphatic vessels. Note that at the short TE around the maximum pre- versus post-Gd blood contrast, positive CSF contrast can also be detected, the magnitude of which is comparable to that of the negative blood contrast at short TE.

In comparison, **Figures 15(c,d)** show the simulation results for the original cDSC MRI approach developed in our previous study (40). Here, the pre- versus post-Gd blood contrast ΔMz/M0 (**Figure 15d**) shows a negative signal change that peaks around TE = 70 ms, but quickly returns to zero at longer TEs (TE > 600 ms). As this sequence was optimized for T2-weighted pre- versus post-CSF contrast ΔMz/M0 (40), a relatively long TR of 9s was chosen, which is too long for measuring blood perfusion. The pre- versus post-Gd CSF contrast ΔMz/M0 (**Figure 15d**) shows a negative signal change for TE > 500ms in this T2-weighted sequence (40) and peaks around TE = 1350 ms. The TE in cDSC MRI was chosen around the time when the CSF contrast peaks and the blood signals (**Figure 15c**) are negligible. The magnitude of the CSF contrast (~0.15) in cDSC MRI is smaller than that in the proposed DDSEP sequence at the long TE (~0.2, **Figure 15b**).

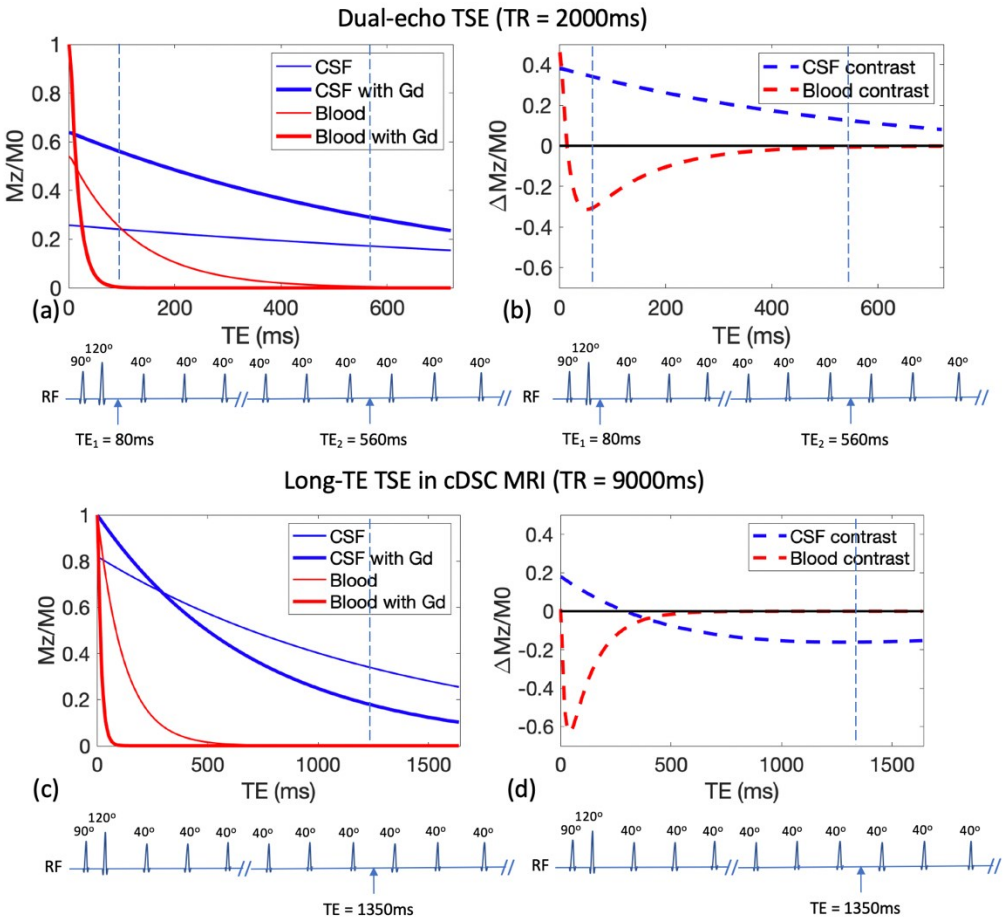

Figure 15: Pulse sequences and simulation resultsfor the proposed dual-echo TSE sequence (a, b), and the long-TE TSE sequence developed in the previous cDSC MRI study (c,d). MR signals in blood and CSF with and without Gd are simulated in (a, c) and the contrast between pre- and post-Gd signals in blood and CSF are shown in (b, d). The fractional MR signals (Mz/M0) and the fractional MR signal changes before and after Gd injection (ΔMz/M0=(Mz_post_Gd-Mz_pre_Gd)/M0) are displayed as functions of TE. The vertical dashed lines indicate the TEs in respective sequences.

In all simulations in **Figure 15**, the concentration of Gd in blood and CSF was fixed based on the literature in healthy human subjects (see Methods). **Figure 16** shows simulation results for the pre- versus post-Gd contrast ΔMz/M0 in blood and CSF as a function of Gd concentration for both sequences. For the blood contrast (**Figure 16a**), the

first echo (TE1) in the proposed DDSEP sequence shows a biphasic relationship with Gd concentration as the contrast is T1-dominant for blood signals. The blood contrast is zero for the second echo (TE2) in DDSEP and the original cDSC MRI as the TE is sufficiently long to suppress the blood signals. In the DDSEP sequence, a theoretical TE = 0 signal can be fitted numerically from the two echoes. At TE = 0, the contrast is only affected by the Gd induced T1 change, which leads to a positive signal change that quickly plateaus with increasing Gd concentration as the post-Gd blood signal approaches zero due to fast T1 decay (thus maximum pre- versus post-Gd contrast). For the CSF contrast (**Figure 16b**), both the first (TE1) and second (TE2) echo in the proposed DDSEP sequence show a biphasic relationship with Gd concentration as the contrast is T1-dominant for the CSF signals in this sequence with a short TR. By contrast, in the original cDSC MRI sequence, the T2-dominant contrast for the CSF signals (40) is always negative and increases in magnitude (more negative) monotonically with Gd concentration, and plateaus for approximately [Gd] > 0.5 mmol/L. At TE = 0 in the DDSEP sequence, similar to the blood contrast, the CSF contrast is also only affected by the Gd induced T1 change, which leads to a positive signal change that quickly plateaus with increasing Gd concentration. It is worth noting that for the typical range of Gd concentration in the CSF (0 - 0.5 mmol/L, shaded in **Figure 16b**) as measured in previous studies (40), only the second echo (TE2) in the proposed DDSEP sequence shows a biphasic relationship between the CSF contrast and Gd concentration, while for all other sequences, the CSF contrast either increases or decreases monotonically with Gd concentration, which makes it possible to determine Gd concentration from the signal changes.

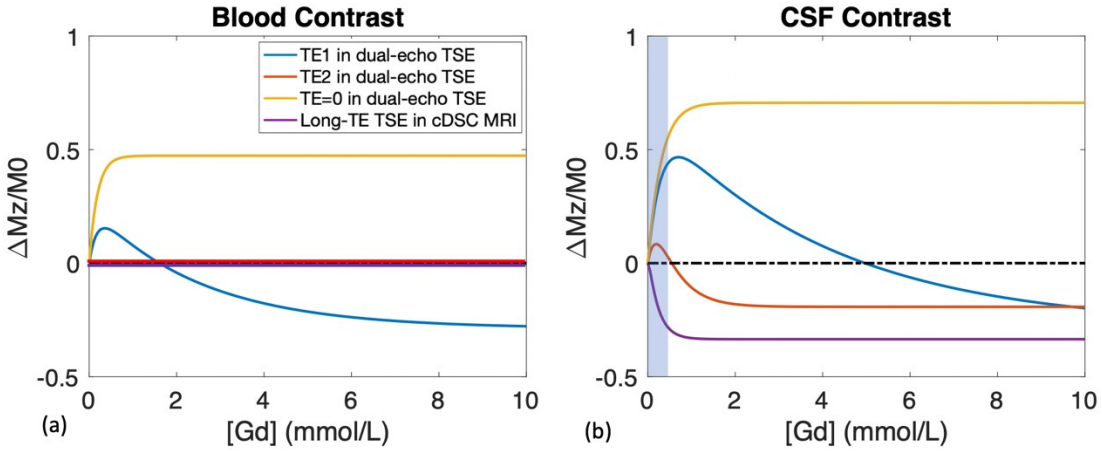

Figure 16: Simulations of the signal contrast with and without Gd in (a) blood and (b) CSF as a function of Gd Concentration ([Gd]) are demonstrated. The imaging parameters adopted in the human experiments are used for this simulation (see Methods). In the proposed dual-echo TSE sequence, signal contrasts at the two acquired TEs (TE1 = 80 ms, TE2 = 560 ms) and the theoretical TE = 0 (which can be numerically fit from TE1 and TE2) are calculated. Signal contrasts in the long-TE TSE in cDSC MRI (TE = 1350 ms) are also simulated.

4.3.2 Human results: perfusion parameters related to blood vessels

Figures 17-20 show typical images and time courses acquired in healthy human subjects on 3T. The quantitative results are compared in **Table 4**.

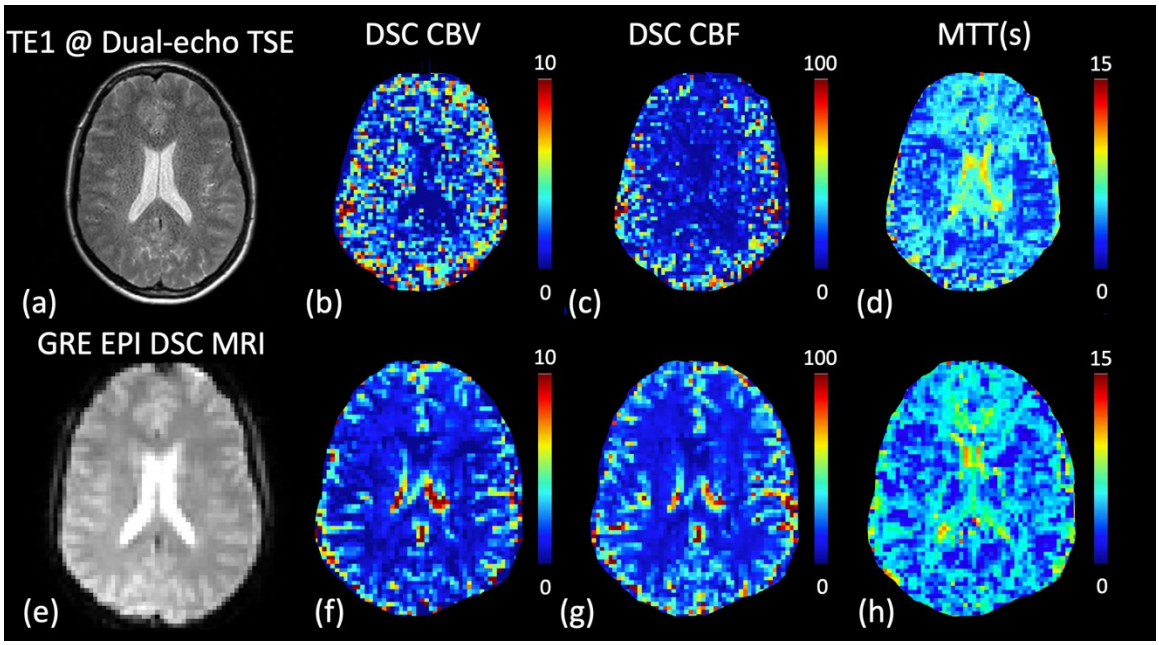

Figure 17: Dual-echo TSE sequence and the standard GRE EPI DSC image. Representative results for the measurement of blood perfusion from human scans using the optimized dual-echo TSE sequence (a-d) and the standard GRE EPI DSC MRI sequence (e-h) on 3T are shown. The raw MR images from the short TE (TE1 = 80 ms) in the proposed dual-echo TSE sequence and from the standard GRE EPI DSC sequence are displayed in (a) and (e), respectively. The derived maps of CBV, CBF, and MTT from each sequence are demonstrated subsequently. Note that the DSC CBV and CBF values are not absolute measures and thus are in arbitrary unit (a.u.). The color bars indicate the corresponding scales of each parameter. Note that the spatial resolution in the dual-echo TSE sequence (1x1x2 mm^3) was higher than the standard GRE EPI DSC sequence (2.8x2.8x5 mm^3). The approximately same slice location is shown in the figure.

.

Figure 17 compares DDSEP images acquired at short TE (**Figure 17a**) with the standard GRE EPI DSC images (**Figure 17f**). The parametric maps of CBV, CBF, and MTT for both methods are also compared. Overall, the contrasts in the corresponding images were comparable between the two methods. Note that the spatial resolution in the proposed approach (1x1x2 mm^3) was much higher than the DSC MRI scans (2.8x2.8x5 mm^3, used in a previous study (90)) as such spatial resolution is preferred for measuring

perfusion in lymphatic vessels at the long TE. The time courses averaged over all grey matter voxels (**Figures 20a,b**) showed a consistent temporal pattern from both methods, reaching maximum contrast ~20s after Gd injection and returning to baseline ~28s after Gd injection. **Table 4** compares average tSNR, CNR, relative signal change (ΔS/S) before and after Gd injection, and perfusion parameters related to blood vessels in grey matter measured by the two approaches from all participants. The magnitude of ΔS/S was greater in the standard GRE EPI DSC MRI method mainly due to its gradient echo based contrast as compared to the spin echo based contrast in the proposed TSE sequence. GRE EPI DSC MRI also showed higher tSNR and CNR than the DDSEP sequence ($P < 0.05$), as is expected from its much larger voxel size (lower spatial resolution) and its gradient echo based contrast. The derived perfusion parameters of CBV, CBF, MTT, $T_{\underline{onset}}$, TTP, and T_{return} in grey matter were consistent between the two approaches ($P > 0.1$), and were in the typical range for healthy human subjects as reported in the literature (13).

4.3.3 Human results: dynamic signal changes in the CSF

Figures 18-19 show typical images acquired using the proposed DDSEP sequence at long TE and the cDSC MRI approach. FLAIR images were used to identify the two ROIs described in Methods, in regions where cerebral lymphatic vessels have been identified in human brains, including around the dural sinuses (superior sagittal sinus) and the cribriform plate (3-5). In both regions, CSF signal changes after Gd injection were detected in FLAIR and in the proposed DDSEP sequences. Maps of several parameters including T_{onset}, TTP, ΔS/S, and Gd concentration in the CSF ([Gd]) extracted from the dynamic signal changes detected with the DDSEP and cDSC sequences are shown for each ROI. The time courses from both ROIs (**Figures 20c-f**) showed a

consistent temporal pattern from both methods, respectively. The CSF signal change after Gd injection detected in both sequences remained preserved for the entire acquisition period (approximately 5 minutes after Gd injection). Note that the ΔS/S in CSF in the DDSEP sequence is expected to be positive (**Figure 15c,d**), whereas ΔS/S in CSF in the original cDSC MRI sequence is expected to be negative (**Figure 15e,f**) due to their T1 and T2 weighting, respectively. Therefore, the absolute values of ΔS/S are compared here.

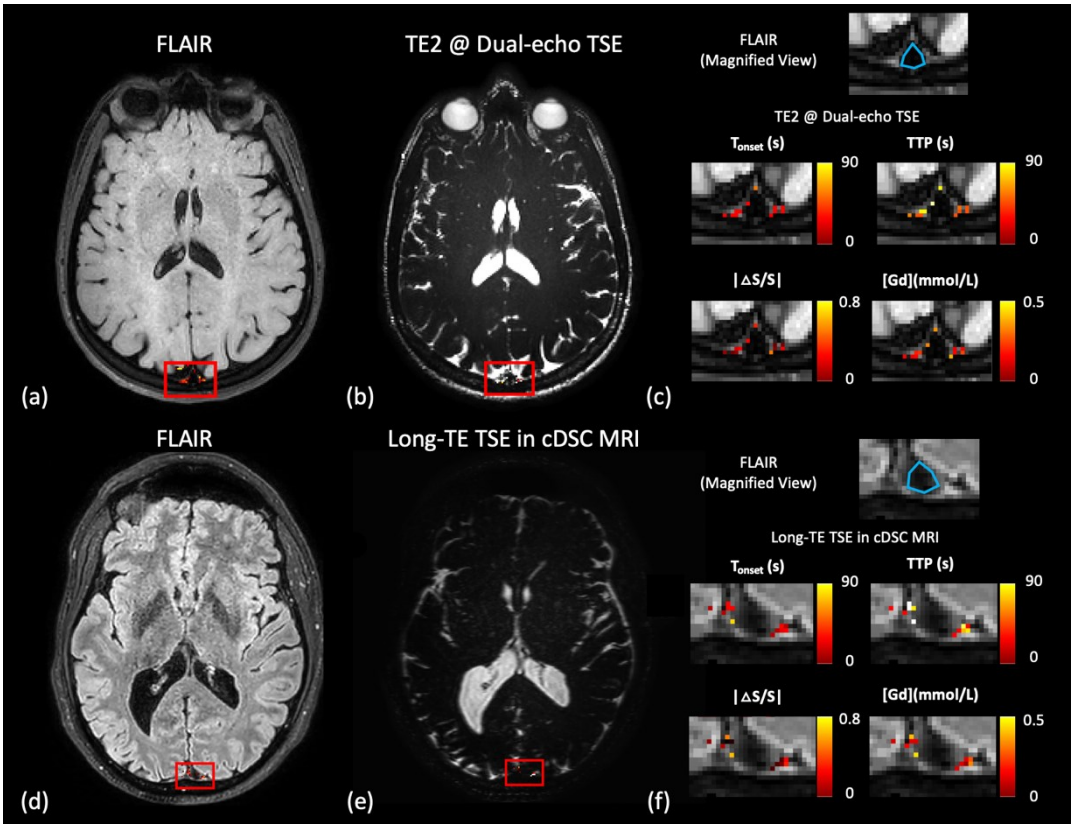

Figure 18: Dual-echo TSE and the long TE TSE images around the dural sinuses. Representative results for the measurement of dynamic signal changes in the CSF from human scans on 3T are shown. The region-of-interest (ROI, red boxes) around the dural sinuses (DS) (especially the superior sagittal sinus) that contains the meningeal lymphatic vessels is manually drawn. (a) The FLAIR image is

shown to confirm the location of the meningeal lymphatic vessels. The relative signal changes (ΔS/S) detected with the FLAIR sequence in the ROI are overlaid on the image. (b) The raw image acquired at the long TE (TE2 = 560 ms) in the proposed dual-echo TSE sequence is shown with ΔS/S overlaid on the image. Only voxels with a contrast-to-noise ratio (CNR) > 1 were highlighted in the image (see Data analysis). (c) A magnified view (axial) of the FLAIR image in the ROI, and maps of the following parameters extracted from the dynamic time courses detected in the dual-echo TSE sequence overlaid on the FLAIR image are shown: T_{onset} = time of onset, TTP = time to peak, absolute value of relative signal change |ΔS/S| between pre- and post-Gd, [Gd] = concentration of Gd. The blue contour on the magnified FLAIR image outlines approximately the location of the superior sagittal sinus, around which the meningeal lymphatic vessels are located in previous studies. The color bars indicate the corresponding scales of each parameter. For comparison, results from the previous cDSC MRI sequence: the FLAIR image, raw cDSC image, and the corresponding parametric maps are shown in (d), (e), and (f), respectively. The slice location was chosen to cover the same ROI (red boxes) around the dural sinuses (DS) (especially the superior sagittal sinus) that contains the meningeal lymphatic vessels.

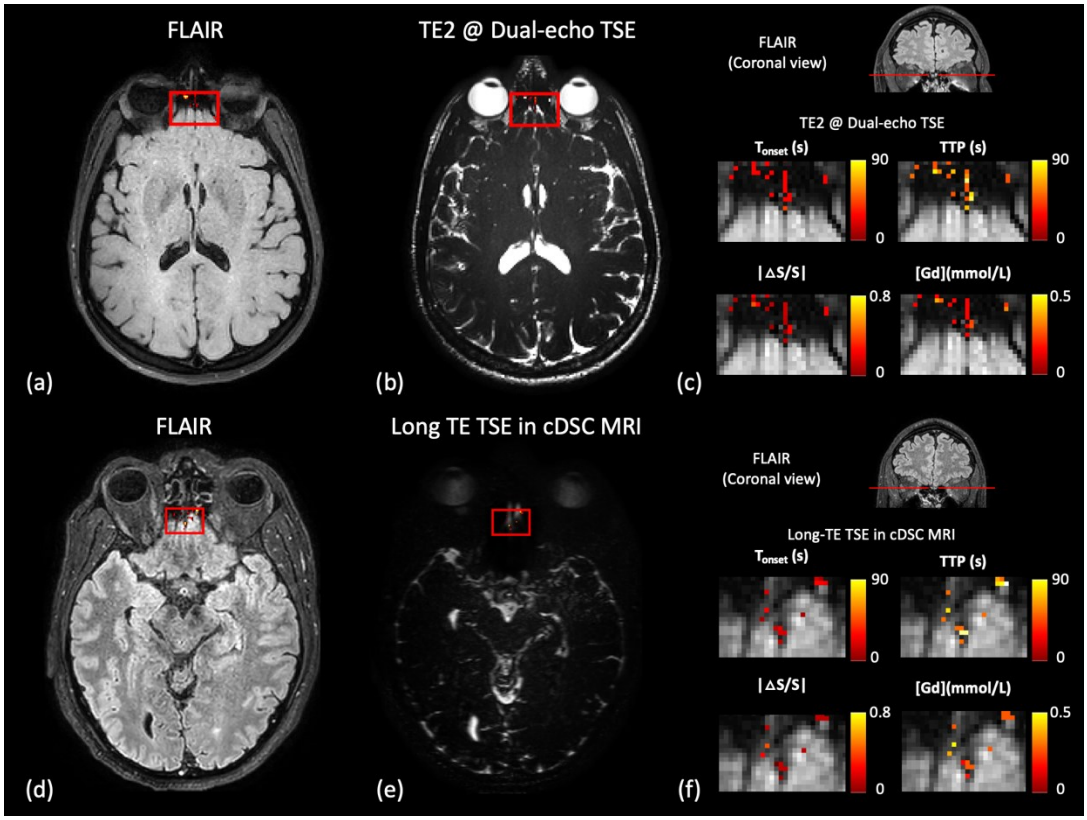

Figure 19: Dual-echo TSE and the long TE TSE images around the cribriform plate. Representative results for the measurement of dynamic signal changes in the CSF from human scans on 3T are shown. The region-of-interest (ROI, red boxes) around the cribriform plate (CP) that contains the olfactory lymphatic vessels are manually drawn. (a) The FLAIR image is shown to confirm the location of the olfactory lymphatic vessels. The relative signal changes (ΔS/S) detected with the FLAIR sequence in the ROI are overlaid on the image. (b) The raw image acquired at the long TE (TE2 = 560 ms) in the proposed dual-echo TSE sequence is shown with ΔS/S overlaid on the image. Only voxels with a contrast-to-noise ratio (CNR) > 1 were highlighted in the image (see Data analysis). (c) A coronal view of the FLAIR image is shown to indicate the location of the axial slice. Maps of the following parameters extracted from the dynamic time courses detected in the dual-echo TSE sequence overlaid on the magnified axial FLAIR image are shown: T_{onset} = time of onset, TTP = time to peak, absolute value of relative signal change |ΔS/S| between pre- and post-Gd, [Gd] = concentration of Gd. The color bars indicate the corresponding scales of each parameter. For comparison, results from the previous cDSC MRI sequence: FLAIR image, raw cDSC image, and the corresponding parametric maps are shown in (d), (e), and (f), respectively. The slice location was chosen to cover the same ROI (red boxes) around the cribriform plate (CP) that contains the olfactory lymphatic vessels.

Table 4 compares average tSNR, CNR and parameters extracted from the dynamic signal changes detected in CSF from the two approaches from all participants. Both approaches showed comparable tSNR ($P > 0.1$). The magnitude of $\Delta S/S$ in CSF was greater in the DDSEP sequence ($P < 0.05$), which leads to a greater CNR for the proposed method ($P < 0.05$). The derived temporal parameters of T_{onset} and TTP, and Gd concentration in CSF were consistent between the two approaches ($P > 0.1$) and in the typical range for healthy human subjects (40).

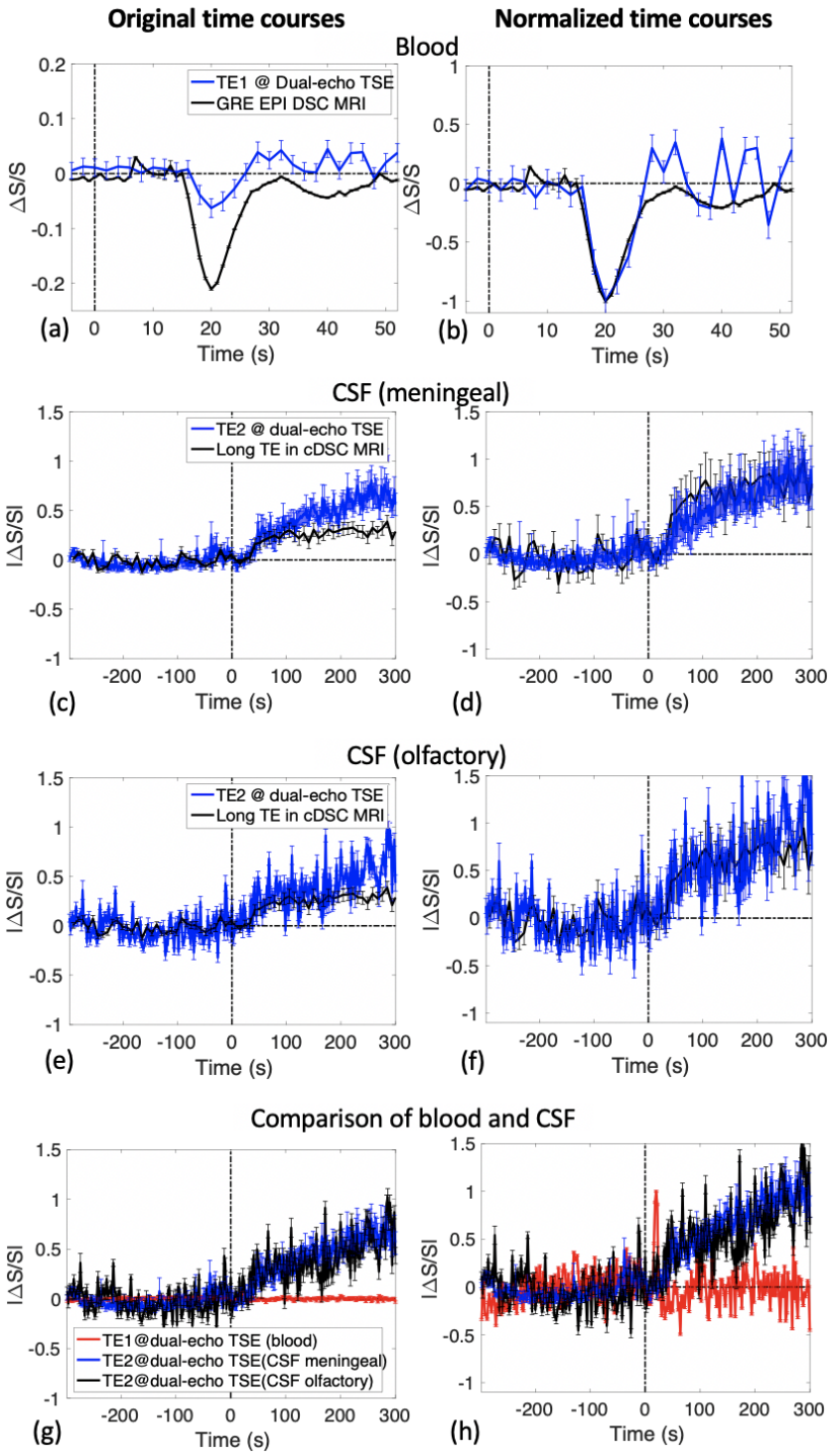

Figure 20: Time courses detected in blood and CSF before and after Gd injectionare shown. The relative signal changes (ΔS/S) between pre- and post-Gd

images are shown as a function of time. The error bars indicate standard deviations. The vertical dotted lines indicate the time when Gd is injected. (a) The average time courses from the blood vessels in grey matter tissue detected using the proposed sequence at short TE (TE1 = 80 ms) and the standard GRE EPI DSC MRI sequence are shown. (b) The same time courses as in (a) normalized by their corresponding peaks (the largest signal change) are shown in order to compare their temporal difference. (c) The average time courses in the meningeal lymphatic vessels around the dural sinuses region detected using the proposed sequence at long TE (TE2 = 560 ms) and the previous cDSC MRI sequence are shown. (d) Normalized time courses from (c). (e) The average time courses in the olfactory lymphatic vessels around the cribriform plate detected using the proposed sequence at long TE (TE2 = 560 ms) and the previous cDSC MRI sequence are shown. (f) Normalized time courses from (e). (g) To compare the time courses in the blood and meningeal and olfactory lymphatic vessels detected using the proposed approach, the same time courses as in (a, c, e) are displayed together. (h) Normalized time courses from (g). Note that in (c-h), the absolute values of relative signal changes (ΔS/S) between pre- and post-Gd images are shown for comparison since ΔS/S from different sequences can have opposite signs.

Table 4: Quantitative results from DDSEP MRI and the existing separate methods(DSC MRI and cDSC MRI for blood and lymphatic vessels, respectively) in healthy subjects (n = 8)

	Separate	**Combined**	**P**
Cerebrovascular perfusion parameters in grey matter tissue			
tSNR	42.7±11.3	13.4±7.6	0.001*
CNR	27.1±3.5	5.2±1.3	< 0.0001*
CBV_{GM}/CBV_{WM}	1.92±0.46	1.88±0.69	0.91
CBF_{GM}/CBF_{WM}	2.31±0.31	2.26±0.74	0.89
MTT (s)	4.73±0.76	4.69±0.89	0.94
ΔS/S	-0.22±0.07	-0.06±0.03	0.0005*
T_{onset} (s)	15.7±0.8	15.6±0.9	0.86
TTP (s)	20.4±0.7	20.3±0.9	0.70
T_{return} (s)	28.2±1.0	28.6±1.4	0.61
Cerebral lymphatic vessels in the region around the dural sinuses (DS)			
tSNR	14.7±4.9	13.6±5.7	0.75
CNR	2.0±0.4	3.1±0.5	0.004*

ΔS/S	-0.28±0.06	0.53±0.12	0.003*
[Gd] (mmol/L)	0.14±0.07	0.16±0.06	0.62
T_{onset} (s)	27.3±8.8	29.8±7.4	0.67
TTP (s)	52.7±22.4	55.4±10.5	0.81
Cerebral lymphatic vessels in the region around the cribriform plate (CP)			
tSNR	10.4±5.5	11.8±3.2	0.64
CNR	1.7±0.5	2.3±0.4	0.05*
ΔS/S	-0.33±0.08	0.49±0.21	0.15
[Gd] (mmol/L)	0.28±0.08	0.23±0.09	0.36
T_{onset} (s)	28.7±23.8	32.3±10.3	0.60
TTP (s)	71.8±32.9	68.9±23.1	0.88

4.3.4 Comparison of the dynamic signal changes in blood and lymphatic vessels

The time courses from blood vessels, and meningeal and olfactory lymphatic vessels measured in the proposed DDSEP sequence at the short (TE1) and long (TE2) echoes, respectively, are shown and compared in **Figures 20g,h**. Only time courses measured using the combined method were compared as they are from the same scans and the same subjects. Since ΔS/S in CSF is expected to be positive and ΔS/S in blood negative, absolute values of ΔS/S were compared here. The magnitude of ΔS/S was smaller in blood than in CSF (**Table 4**, $P < 0.05$). The time of onset (T_{onset}) and time to peak (TTP) were both shorter in blood than in CSF (**Table 4**, $P < 0.05$). The blood time courses quickly returned to baseline whereas the CSF time courses did not return to baseline for the duration of our experiments (approximately 5 minutes after Gd injection). The time of return (T_{return}) for blood signals was comparable to the time of onset (T_{onset}) for

CSF signals (**Table 4**, P > 0.1), and was significantly shorter than the time to peak (TTP) for CSF signals (**Table 4**, P < 0.01).

4.4 Discussion

To date, most existing MRI approaches can only measure perfusion parameters related to blood or lymphatic vessels separately, and most contrast enhanced MRI methods are optimized for detecting Gd-induced signal changes in the blood (13). In the current study, we demonstrate a dual-echo TSE sequence (DDSEP MRI) with optimized contrasts for the detection of Gd induced MR signal changes in the blood and CSF with short (80 ms) and long (560 ms) TE, respectively. A primary advantage of the proposed approach is that it provides a tool for concurrent measurement of perfusion parameters related to both blood and lymphatic vessels in the brain in one single scan, which substantially shortens the total scan time and reduces inter-scan confounding effects from physiological variations. In addition, the dose of contrast medium needed is halved. Importantly, this approach can be used to study the interaction between the microvascular and lymphatic systems in the brain, which plays a critical role in the regulation of blood supply and waste clearance in the brain and has been linked to a number of brain diseases (23,24,26). Our initial results in healthy human subjects demonstrated that consistent perfusion parameters related to blood and lymphatic vessels can be measured by the proposed combined approach and the respective existing separate methods in the human brain.

Multi-echo based MRI approaches have been employed in DSC and dynamic contrast enhancement (DCE) MRI. Dual gradient echo (GRE) based methods have been

developed to provide both perfusion (DSC) and vascular permeability (DCE) measures using a single dose of Gd contrast (91-95). The PERfusion with Multiple Echoes and Temporal Enhancement (PERMEATE) method is a dual GRE multi-shot EPI sequence developed to improve R2* quantification and to reduce geometric distortion in typical EPI images (96,97). The Spiral Perfusion Imaging with Consecutive Echoes (SPICE) method is another dual GRE approach using a spiral readout (98). The spin- and gradient-echo (SAGE) sequence combines the acquisition of two GREs, two asymmetric spin echoes, and a single spin echo (99-102) to provide probably a most complete set of hemodynamic parameters related to macro- and microvascular perfusion, vascular permeability, and other properties within a single acquisition (99-103). The simplified SAGE (sSAGE) approach reduces the acquisition to two GREs and a single spin echo, making it more feasible for clinical use (103,104). The key difference in the proposed DDSEP approach is that it is a dual-spin-echo sequence with a long second TE in order to get a pure CSF signal. Thus, the proposed DDSEP sequence furnishes a T1-dominat contrast in the CSF similar to DCE MRI and a T2-dominant contrast in the blood same as DSC MRI. In principle, fast GRE sequences commonly used in standard DCE MRI can provide a T1-dominant CSF contrast as well with some degree of residual T2* effects depending on the TE used. If acquired at multiple gradient echoes, such residual T2* effects can be eliminated by numerically fitting the multi-echo data to an effective TE of 0, thus providing a pure T1 contrast in the CSF. In such fast GRE sequences, both blood and CSF signals are expected to increase after Gd injection. By contrast, in the proposed DDSEP method, the blood and CSF signals show opposite contrasts after Gd injection. Moreover, a main reason for choosing a dual-spin-echo sequence in the proposed DDSEP method that it is known to have better spatial specificity for Gd-induced signal changes in small vessels

than GRE-based sequences (38,68,88,89), which is critical for the method since cerebral lymphatic vessels often run alongside small blood vessels in the brain (3-5).

The long-TE images in the proposed DDSEP approach provide a clean CSF signal with brain parenchyma and blood signals all suppressed due to T2 decay. Thus, the partial volume effects from brain parenchyma and blood are expected to be minimal in the long-TE CSF images. Therefore, even if the spatial resolution (voxel size) is larger than the dimensions of the target structures (the CSF space and the cerebral lymphatic vessels), dynamic signal changes in the CSF can still be measured with the proposed method. On the other hand, the short-TE images in the proposed DDSEP approach are expected to have a negative and a positive contrast for the blood and CSF signals respectively (see simulations in **Figure 15b**). When the spatial resolution is sufficiently fine to separate the blood and lymphatic vessels, or when imaging brain regions that are expected to have only one type of the microvessels, the short-TE images alone can provide measures of dynamic signal changes in both blood and CSF. However, if the voxel contains both blood and lymphatic vessels, the opposite signal changes in blood and CSF will cancel out with each other, resulting in partial volume effects. As cerebral lymphatic vessels can only be found in several specific brain regions, such partial volume effects in the blood signals in most GM and WM regions are expected to be small. For the CSF signals, the long TE images are required to separate the partial volume effects from blood.

The Gd-induced signal changes in the blood and CSF can be further separated by their differential temporal profiles. According to the data measured in the current study in healthy human subjects (**Figures 20 g,h** and **Table 4**), after Gd injection, the blood signals decreased and then quickly restored to baseline before significant changes can be measured in the CSF signals. To the best our knowledge, this may be the first time that

dynamic signal changes in small blood and lymphatic vessels in the human brain are measured in the same subjects. The timing parameters measured in the blood and CSF time courses are congruent with the DSC literature (13) and our previous study using cDSC MRI (40), respectively. The timing difference between the blood and CSF signal changes seems to support the hypothesis that after intravenous (IV) injection, the Gd-based contrast agents enter the CSF space via the dural blood vessel wall that lacks a BBB (15-18). This timing difference is also comparable to the timing of signal changes reported in many brain tumor studies using DCE MRI where Gd-based contrast agents often leak out from the impaired BBB in the tumor region (84,85). The exact mechanism for such communication between dural blood vessels and meningeal lymphatic vessels in the parasagittal dura is still under extensive investigation (35). In that regard, the proposed DDSEP approach will be performed around the parasagittal dura region in subsequent studies in order to examine the pathway for Gd-based contrast agents to travel from dural blood vessels to meningeal lymphatic vessels in the human brain.

The timing difference between the blood and CSF signal changes also enables us to estimate Gd concentration ([Gd]) in the CSF using the proposed DDSEP MRI approach. In the original cDSC MRI, Gd concentration can be uniquely determined from the T2-dominant CSF contrast (40). However, the T1-dominant contrast for CSF from the long-TE images in DDSEP MRI has a bi-phasic relationship with Gd concentration (**Figure 16b**), which makes it uncertain to estimate [Gd] from the long-TE images alone. Signal changes from the short-TE images in DDSEP MRI have a monotonic relationship with Gd concentration for both blood and CSF (**Figure 16**) when the Gd concentration is within the typical range expected in the human brain after intravenous (IV) injection of a standard dose of Gd-based contrast agents. With the significant timing difference between the blood

and CSF signal changes detected in our data, the blood signal changes can be assumed to be 0 when the CSF signal changes reach the peak. This temporal separation allows us to determine Gd concentration from the short-TE images acquired around the CSF TTP in DDSEP MRI. In our data, the Gd concentration in CSF estimated using the new DDSEP MRI approach was in agreement with the results from our previous study using the cDSC MRI method (40). The Gd concentration in CSF was approximately one fifth of that in blood after IV Gd injection in healthy human subjects.

4.5 Technical limitation and future direction

As a first proof-of-concept study, the proposed DDSEP MRI approach was implemented in multi-slice acquisition mode with 3 slices covering the superior sagittal sinus and the olfactory regions where cerebral lymphatic vessels have been identified. Dynamic signal changes from both blood and lymphatic vessels were detected using DDSEP MRI, based on which we can further optimize and develop the DDSEP MRI sequence in subsequent studies. Although cerebral lymphatic vessels are only identified in several specific brain regions, a whole brain coverage would still be ideal for DDSEP MRI. The main limiting factor here is the long TE (> 500 ms) required for a clean CSF signal and a short TR (< 2 s) required for tracking the dynamic phase of the blood signal. With the multi-slice acquisition mode, only 3 slices can be fit into a TR of 2 s in the current study. A few approaches can be employed to improve the spatial coverage in future studies. First, the flip angles of the readout RF pulse train in the TSE sequence can be optimized to make the required long TE shorter for a complete suppression of blood signals. Second, a three-dimension (3D) acquisition mode with lower spatial resolution

can be used instead of the current multi-slice mode. The 3D mode will allow more acceleration using advanced fast imaging techniques such as the Compressed-Sensing SENSE (CS-SENSE) technique (47,69) as in our previous study (40) to improve the spatial coverage with the same readout time. In DDSEP MRI, the short-TE images are mainly used to measure blood perfusion similar to DSC MRI, which is typically performed at a much lower spatial resolution (2-3mm instead of 1mm currently). The spatial resolution for the long-TE images in DDSEP MRI can also be reduced substantially because negligible partial volume effects are expected with blood and parenchymal signals suppressed. Finally, based on our data in healthy human subjects, the dynamic phases for blood and CSF signal changes after intravenous (IV) Gd administration have a significant temporal separation. As the short-TE images can detect Gd-induced signal changes in both blood and CSF as shown in the simulations (**Figure 15b**), such temporal separation seems to eliminate the need for the long-TE images in DDSEP MRI, which will significantly shorten the acquisition time. Furthermore, different readout sequences can be optimized for the blood and CSF phases, respectively. All these options discussed above will be evaluated in our follow-up study.

In addition to CBV and CBF, measures related to the BBB permeability are quite useful in various brain diseases. In the current DDSEP MRI sequence, the short TE is chosen to produce T2-weighted images for the blood signals. Therefore, the K2 parameter from DSC MRI can be calculated using the short-TE images provided sufficient SNR is achieved. However, the more commonly used K_{trans} parameter for permeability from DCE MRI would need a T1-weighted blood contrast. To obtain such T1-weighted blood contrast, images need to be acquired at a TE much shorter than the current TE1 (= 80 ms). Alternatively, one can also acquire images at an additional TE in the intermediate

range (100-300 ms), and numerically fit for an effective TE of 0 using data from both echoes. The long TE in the current DDSEP MRI sequence is too long for blood signals which have already decayed to almost zero, and thus cannot be used for multi-echo fitting. These technical development is being pursued in follow-up studies.

In summary, we demonstrated the DDSEP MRI approach based on a dual-echo TSE sequence which can measure perfusion parameters related to both small blood and lymphatic vessels concurrently after intravenous (IV) injection of Gd contrast medium in healthy human subjects. The results from the DDSEP MRI method are in line with previous studies using separate methods for small blood and lymphatic vessels, respectively. Interestingly, signal changes from small blood vessels occurred much faster than those from the CSF and cerebral lymphatic vessels. To the best of our knowledge, this may be the first study in which such interaction was measured and reported in the same human subjects. The proposed methodology is being further developed to expand its spatial coverage to the whole brain. Given the importance of the microvascular and cerebral lymphatic systems in the brain and their tight interaction, we believe that the proposed DDSEP MRI approach may provide a useful tool for studies on these systems in the healthy brain and various brain diseases.

Chapter 5

5. Conclusion and future work

In summary, we demonstrated that CS-SENSE showed superior SNR than SENSE in MPRAGE and TSE scans performed with high acceleration factors (R=0-28) on phantoms and human brains. The spatial blurring effects evaluated by the FWHM of PSF were comparable between CS-SENSE and SENSE and were negligible for R<=16. Significant foldover artifacts only occurred in SENSE images. Based on these results, CS-SENSE appears to be the favored parallel imaging technique compared to SENSE, and the acceleration factor R can be pushed up to around 16 for highly accelerated acquisitions with a 32-channel receiver array coil.

With the high acceleration of MRI acquisition using CS-SENSE, we demonstrated that dynamic signal changes induced by the distribution of Gd contrast medium in the CSF can be detected in healthy human subjects with an optimized 3D TSE sequence. The concentration of Gd in the CSF can be quantified from the relative signal change in this approach. The proposed cDSC methodology does not rely on any particular theory on CSF circulation in the human brain. We expect it to be a useful tool for human and animal studies on CSF circulation and cerebral lymphatic vessels in the brain using contrast agent based approaches.

We also demonstrated the DDSEP MRI approach based on a dual-echo TSE sequence which can measure perfusion parameters related to both small blood and lymphatic vessels concurrently after intravenous (IV) injection of Gd contrast medium in healthy human subjects. The results from the DDSEP MRI method are in line with previous studies using separate methods for small blood and lymphatic vessels, respectively. Interestingly, signal changes from small blood vessels occurred much faster than those from the CSF and cerebral lymphatic vessels. To the best of our knowledge, this may be the first study in which such interaction was measured and reported in the same human subjects. The proposed DDSEP methodology is being further developed to expand its spatial coverage to the whole brain. Given the importance of the microvascular and cerebral lymphatic systems in the brain and their tight interaction, we believe that the proposed DDSEP MRI approach may provide a useful tool for studies on these systems in the healthy brain and various brain diseases.

The cDSC MRI method has been applied to investigate lymphatic vessels in healthy human subjects in the following regions. We have collected whole brain data and the analysis is on-going for: olfactory regions, optic nerve, spinal nerve, choroid plexus, and inner ear. In addition, we are also analyzing data from MCI and PD patients. The proposed methods have also been implemented on Bruker small animal MRI systems. On-going studies include studying lymphatic vessels in wild type (WT), Parkinson's Disease(PD), Huntington's Disease (HD), Alzheimer's Disease (AD) and obesity mouse models. The proposed methods have been used in a canine model for hydrocephalus on human 3T MRI scanners.

Appendix A

1. Signal equations in the proposed 3D TSE sequence.

The MR signals detected with a 3D TSE sequence can be described with:

$$S = (1 - e^{-\frac{TR}{T1}}) \times e^{-\frac{TE}{T2}} \quad [S1]$$

Note that TE here represents the effective echo time which is determined by the readout echo train in the sequence (67).

The Gd induced changes in T1 and T2 relaxation times can be written as:

$$\frac{1}{T1_{Gd}} = \frac{1}{T1_0} + r_1 \times [Gd] \quad [S2]$$

$$\frac{1}{T2_{Gd}} = \frac{1}{T2_0} + r_2 \times [Gd] \quad [S3]$$

where variables with the subscription "0" ($T1_0$ and $T2_0$) represent the values before Gd injection, variables with the subscription "Gd" ($T1_{Gd}$ and $T2_{Gd}$) represent the values after Gd injection, r1 and r2 are the relaxivity of Gd in a certain medium (CSF or blood), and [Gd] is the concentration of Gd in the medium.

The absolute signal change (ΔS) before and after Gd injection is defined as (same as Eq. [1] in Methods):

$$\Delta S = S_{Gd} - S_0 = \left(1 - e^{-\frac{TR}{T1_{Gd}}}\right) \times e^{-\frac{TE}{T2_{Gd}}} - \left(1 - e^{-\frac{TR}{T1_0}}\right) \times e^{-\frac{TE}{T2_0}}, \quad [S4]$$

The relative signal change (ΔS/S) before and after Gd injection is defined as:

$$\frac{\Delta S}{S} = \frac{(S_{Gd} - S_0)}{S_0}, \quad [S5]$$

which can be rewritten as the following according to Eq. [S1]:

$$\frac{\Delta S}{S} = \frac{(1-e^{-\frac{TR}{T1_{Gd}}})\times e^{-\frac{TE}{T2_{Gd}}}}{(1-e^{-\frac{TR}{T1_0}})\times e^{-\frac{TE}{T2_0}}} - 1 \ , \qquad \text{[S6]}$$

and can be rearranged as the following according to Eq. [S3]:

$$\frac{\Delta S}{S} = \frac{(1-e^{-\frac{TR}{T1_{Gd}}})}{(1-e^{-\frac{TR}{T1_0}})} \times \ e^{-TE\times r_2\times[Gd]} - 1 \qquad \text{[S7]}$$

When TR is sufficiently long, it can be simplified to:

$$\frac{\Delta S}{S} = e^{-TE\times r_2\times[Gd]} - 1 \qquad \text{[S8]}$$

Table S1. Simulation results of the proposed 3D TSE sequences on 3T and 7T.

(a) 3T, T1-dominant 3D TSE

			at Maximum Contrast		
Shot Number	**Shortest TE (ms) [a]**	**Maximum Contrast (Mz/M0) [b]**	**CSF signal without Gd (Mz/M0) [c]**	**TR (ms) [d]**	**Volume TR (ms) [e]**
1	1391	0.006	0.044	4592	4592
2	945	0.039	0.110	3761	7522
3	709	0.079	0.164	3352	10056
4	576	0.111	0.204	3153	12612
5	482	0.138	0.241	3069	15345
6	418	0.161	0.266	2975	17850
7	368	0.197	0.259	2829	19803
8	331	0.197	0.297	2817	22536
12	238	0.264	0.296	2538	30456
16	189	0.267	0.371	2692	43072

(b) 3T, T2-dominant 3D TSE

Shot Number[f]	TR (ms) [f]	at Maximum Contrast		
		Maximum Contrast (Mz/M0) [b]	CSF signal without Gd (Mz/M0) [c]	TE (ms) [g]
1	6000	-0.039	0.080	2121
1	7000	-0.064	0.130	1874
1	8000	-0.089	0.181	1676
1	9000	-0.113	0.230	1522
1	10000	-0.135	0.275	1404
1	11000	-0.154	0.314	1311
1	12000	-0.170	0.347	1241
1	13000	-0.184	0.375	1188
1	14000	-0.195	0.398	1144
1	15000	-0.204	0.418	1109
1	20000	-0.229	0.470	1025

(c) 7T, T1-dominant 3D TSE

Shot Number	Shortest TE (ms) [a]	Maximum Contrast (Mz/M0) [b]	at Maximum Contrast		
			CSF signal without Gd (Mz/M0) [c]	TR (ms) [d]	Volume TR (ms) [e]
1	1232	0.011	0.042	5143	5143
2	832	0.048	0.103	4175	8350
3	631	0.089	0.149	3688	11064
4	512	0.123	0.184	3420	13680
5	432	0.148	0.211	3206	16030
6	375	0.176	0.228	3082	18492
7	331	0.199	0.237	2913	20391
8	298	0.216	0.255	2884	23072
12	216	0.253	0.307	2760	33120
16	172	0.280	0.332	2691	43056

(d) 7T, T2-dominant 3D TSE

Shot Number[f]	TR (ms) [f]	Maximum Contrast (Mz/M0) [b]	at Maximum Contrast	
			CSF signal without Gd (Mz/M0) [c]	TE (ms) [g]
1	6000	-0.015	0.038	2049
1	7000	-0.030	0.075	1772
1	8000	-0.048	0.117	1551
1	9000	-0.066	0.162	1382
1	10000	-0.084	0.206	1246
1	11000	-0.100	0.247	1142
1	12000	-0.115	0.284	1062
1	13000	-0.128	0.316	996
1	14000	-0.139	0.343	949
1	15000	-0.149	0.366	912
1	20000	-0.175	0.431	813

[a] Shortest TE determined by the readout train (shot number) was used, as longer TE will further reduce CSF signals with little improvement for the contrast in CSF with and without Gd in the T1-dominant sequence.

[b] Defined in Eq. [1], which reflects the contrast in CSF with and without Gd (Figure 1).

[c] The CSF signal without Gd reflects the baseline signal-to-noise ratio (SNR).

[d] TR that corresponds to the maximum contrast before and after Gd injection (Figure 1).

[e] Volume TR = (shot number) x TR.

[f] In T2-dominant sequences, as long TR is preferred for T2-weighting, only single shot results are shown.

[g] TE that corresponds to the maximum contrast before and after Gd injection (Figure 1).

Appendix B

MR signal equations in the proposed dual-echo TSE MRI sequence:

The MR signal (S) measured in a TSE sequence is related to the magnetization (M_z) with the following equation:

$$S \sim M_z = M_0 \times (1 - e^{-\frac{TR}{T1}}) \times e^{-\frac{TE}{T2}} \quad \text{[S1]}$$

in which M_0 is the equilibrium longitudinal magnetizations. Note that TE here represents the effective echo time which is determined by the readout echo train in the sequence (67).

The Gd induced changes in T1 and T2 relaxation times can be written as:

$$\frac{1}{T1_{Gd}} = \frac{1}{T1_0} + r_1 \times [Gd] \quad \text{[S2]}$$

$$\frac{1}{T2_{Gd}} = \frac{1}{T2_0} + r_2 \times [Gd] \quad \text{[S3]}$$

where variables with the subscription "0" ($T1_0$ and $T2_0$) represent the values before Gd injection, variables with the subscription "Gd" ($T1_{Gd}$ and $T2_{Gd}$) represent the values after Gd injection, r1 and r2 are the relaxivity of Gd in a certain medium (CSF or blood), and [Gd] is the concentration of Gd in the medium.

In the proposed dual-echo TSE sequence, the MR signal measure at the short TE (TE1) can be written as:

Before Gd injection:

$$S1_0 \sim X_{blood} \times C_{blood} \times M_{blood} + X_{CSF} \times C_{CSF} \times M_{CSF} + (1 - X_{blood} - X_{CSF}) \times C_{tissue} \times M_{tissue} \quad \text{[S4a]}$$

After Gd injection:

$$S1_{Gd} \sim X_{blood} \times C_{blood} \times M_{blood,Gd} + X_{CSF} \times C_{CSF} \times M_{CSF,Gd} + (1 - X_{blood} - X_{CSF}) \times C_{tissue} \times M_{tissue} \quad \text{[S4b]}$$

where Xi (i = blood, CSF) is the compartmental fraction (ranging from 0 to 1), Ci (i = blood, CSF, tissue) is the water density for each compartment, and Mi (i = blood, CSF, tissue) is defined in Eq. [S1] with respective T1 and T2 values.

At the long TE (TE2) in the proposed dual-echo TSE sequence, MR signals from blood and tissue can be assumed zero due to T2 delay. Therefore, the equations can be simplified to:

$$S2_0 \sim X_{CSF} \times C_{CSF} \times M_{CSF} = X_{CSF} \times C_{CSF} \times M_0 \times (1 - e^{-\frac{TR}{T1,CSF,0}}) \times e^{-\frac{TE2}{T2,CSF,0}} \quad \text{[S4c]}$$

$$S2_{Gd} \sim X_{CSF} \times C_{CSF} \times M_{CSF,Gd} = X_{CSF} \times C_{CSF} \times M_0 \times (1 - e^{-\frac{TR}{T1,CSF,Gd}}) \times e^{-\frac{TE2}{T2,CSF,Gd}} \quad \text{[S4d]}$$

There are two unknown variables in Eqs. [S4c,d]: X_{CSF} and [Gd] (which gives rise to $T_{1,CSF,Gd}$ and $T_{2,CSF,Gd}$). Therefore, in principle, with the two measures $S2_0$ and $S2_{Gd}$, X_{CSF} and [Gd] can be obtained from Eqs. [S4c,d]. However, because $S2_{Gd}$ has a biphasic relationship with [Gd], [Gd] cannot be uniquely determined with $S2_{Gd}$ alone.

On the other hand, within the range of [Gd] (0-0.5 mmol/L) expected in the CSF and cerebral lymphatic vessels in the human brain after intravenous (IV) Gd administration with a standard dose, $S1_{Gd}$ increases with [Gd] monotonically (see simulation results presented in **Figure 16b**). Furthermore, as shown in our data from healthy human subjects in **Figure 20**, the blood and CSF signal changes showed

significant temporal separation for at least 20 seconds. When the CSF signals showed significant Gd-induced changes, the blood signals have returned to its pre-Gd level. Therefore, M_{blood} in $S1_0$ and $M_{blood,Gd}$ in $S1_{Gd}$ can be assumed the same 30 seconds after Gd injection. Based on these assumptions, the absolute signal change (ΔS) before and after Gd injection measured at TE1 can be defined as:

$$\Delta S1 = S1_{Gd} - S1_0 \sim X_{CSF} \times C_{CSF} \times \left(M_{CSF,Gd} - M_{CSF}\right) = X_{CSF} \times C_{CSF} \times M_0 \times$$

$$\left[\left(1 - e^{-\frac{TR}{T1_{CSF,Gd}}}\right) \times e^{-\frac{TE1}{T2_{CSF,Gd}}} - \left(1 - e^{-\frac{TR}{T1_{CSF,0}}}\right) \times e^{-\frac{TE1}{T2_{CSF,0}}}\right] \quad [S5]$$

Because ΔS1 has a monotonic relationship with [Gd] (**Figure 16b**), [Gd] can be uniquely solved from $\Delta S1/S2_0$:

$$\frac{\Delta S1}{S2_0} = \frac{\left(1-e^{-\frac{TR}{T1_{CSF,Gd}}}\right)\times e^{-\frac{TE1}{T2_{CSF,Gd}}} - \left(1-e^{-\frac{TR}{T1_{CSF,0}}}\right)\times e^{-\frac{TE1}{T2_{CSF,0}}}}{\left(1-e^{-\frac{TR}{T1_{CSF,0}}}\right)\times e^{-\frac{TE2}{T2_{CSF,0}}}} \quad [S6]$$

Note that $S2_0$ can be obtained from the long TE (TE2) in the proposed dual-echo TSE sequence, or it can simply be acquired using a separate scan with the same parameters before Gd injection.

Bibliography

1. Wright BL, Lai JT, Sinclair AJ. Cerebrospinal fluid and lumbar puncture: a practical review. J Neurol 2012;259(8):1530-1545.
2. Sakka L, Coll G, Chazal J. Anatomy and physiology of cerebrospinal fluid. Eur Ann Otorhinolaryngol Head Neck Dis 2011;128(6):309-316.
3. Aspelund A, Antila S, Proulx ST, Karlsen TV, Karaman S, Detmar M, Wiig H, Alitalo K. A dural lymphatic vascular system that drains brain interstitial fluid and macromolecules. The Journal of experimental medicine 2015;212(7):991-999.
4. Louveau A, Smirnov I, Keyes TJ, Eccles JD, Rouhani SJ, Peske JD, Derecki NC, Castle D, Mandell JW, Lee KS, Harris TH, Kipnis J. Structural and functional features of central nervous system lymphatic vessels. Nature 2015;523(7560):337-341.
5. Absinta M, Ha SK, Nair G, Sati P, Luciano NJ, Palisoc M, Louveau A, Zaghloul KA, Pittaluga S, Kipnis J, Reich DS. Human and nonhuman primate meninges harbor lymphatic vessels that can be visualized noninvasively by MRI. eLife 2017;6.
6. Ahn JH, Cho H, Kim JH, Kim SH, Ham JS, Park I, Suh SH, Hong SP, Song JH, Hong YK, Jeong Y, Park SH, Koh GY. Meningeal lymphatic vessels at the skull base drain cerebrospinal fluid. Nature 2019;572(7767):62-66.
7. Patel TK, Habimana-Griffin L, Gao X, Xu B, Achilefu S, Alitalo K, McKee CA, Sheehan PW, Musiek ES, Xiong C, Coble D, Holtzman DM. Dural lymphatics regulate clearance of extracellular tau from the CNS. Mol Neurodegener 2019;14(1):11.
8. Da Mesquita S, Fu Z, Kipnis J. The Meningeal Lymphatic System: A New Player in Neurophysiology. Neuron 2018;100(2):375-388.
9. Louveau A, Herz J, Alme MN, Salvador AF, Dong MQ, Viar KE, Herod SG, Knopp J, Setliff JC, Lupi AL, Da Mesquita S, Frost EL, Gaultier A, Harris TH, Cao R, Hu S, Lukens JR, Smirnov I, Overall CC, Oliver G, Kipnis J. CNS lymphatic drainage and neuroinflammation are regulated by meningeal lymphatic vasculature. Nat Neurosci 2018;21(10):1380-1391.
10. Da Mesquita S, Louveau A, Vaccari A, Smirnov I, Cornelison RC, Kingsmore KM, Contarino C, Onengut-Gumuscu S, Farber E, Raper D, Viar KE, Powell RD, Baker W, Dabhi N, Bai R, Cao R, Hu S, Rich SS, Munson JM, Lopes MB, Overall CC, Acton ST, Kipnis J. Functional aspects of meningeal lymphatics in ageing and Alzheimer's disease. Nature 2018;560(7717):185-191.
11. Antila S, Karaman S, Nurmi H, Airavaara M, Voutilainen MH, Mathivet T, Chilov D, Li Z, Koppinen T, Park JH, Fang S, Aspelund A, Saarma M, Eichmann A, Thomas JL, Alitalo K. Development and plasticity of meningeal lymphatic vessels. The Journal of experimental medicine 2017;214(12):3645-3667.

12. Tarasoff-Conway JM, Carare RO, Osorio RS, Glodzik L, Butler T, Fieremans E, Axel L, Rusinek H, Nicholson C, Zlokovic BV, Frangione B, Blennow K, Menard J, Zetterberg H, Wisniewski T, de Leon MJ. Clearance systems in the brain-implications for Alzheimer disease. Nat Rev Neurol 2015;11(8):457-470.
13. Quarles CC, Bell LC, Stokes AM. Imaging vascular and hemodynamic features of the brain using dynamic susceptibility contrast and dynamic contrast enhanced MRI. Neuroimage 2019;187:32-55.
14. Kennan RP, Jager HR. T2- and T*2 -w DCE-MRI: Blood Perfusion and Volume Estimation using Bolus Tracking. Quantitative MRI of the Brain: Measuring Changes Caused by Disease. Hoboken: John Wiley & Sons, Ltd; 2003. p 365.
15. Antony J, Hacking C, Jeffree RL. Pachymeningeal enhancement-a comprehensive review of literature. Neurosurg Rev 2015;38(4):649-659.
16. Sze G, Soletsky S, Bronen R, Krol G. MR imaging of the cranial meninges with emphasis on contrast enhancement and meningeal carcinomatosis. AJNR Am J Neuroradiol 1989;10(5):965-975.
17. George U, Rathore S, Pandian JD, Singh Y. Diffuse pachymeningeal enhancement and subdural and subarachnoid space opacification on delayed postcontrast fluid-attenuated inversion recovery imaging in spontaneous intracranial hypotension: visualizing the Monro-Kellie hypothesis. AJNR Am J Neuroradiol 2011;32(1):E16.
18. Smirniotopoulos JG, Murphy FM, Rushing EJ, Rees JH, Schroeder JW. Patterns of contrast enhancement in the brain and meninges. Radiographics : a review publication of the Radiological Society of North America, Inc 2007;27(2):525-551.
19. Eide PK, Ringstad G. Delayed clearance of cerebrospinal fluid tracer from entorhinal cortex in idiopathic normal pressure hydrocephalus: A glymphatic magnetic resonance imaging study. J Cereb Blood Flow Metab 2019;39(7):1355-1368.
20. Eide PK, Vatnehol SAS, Emblem KE, Ringstad G. Magnetic resonance imaging provides evidence of glymphatic drainage from human brain to cervical lymph nodes. Scientific reports 2018;8(1):7194.
21. Ringstad G, Valnes LM, Dale AM, Pripp AH, Vatnehol SS, Emblem KE, Mardal KA, Eide PK. Brain-wide glymphatic enhancement and clearance in humans assessed with MRI. JCI insight 2018;3(13).
22. Ringstad G, Vatnehol SAS, Eide PK. Glymphatic MRI in idiopathic normal pressure hydrocephalus. Brain 2017;140(10):2691-2705.
23. Iliff JJ, Lee H, Yu M, Feng T, Logan J, Nedergaard M, Benveniste H. Brain-wide pathway for waste clearance captured by contrast-enhanced MRI. J Clin Invest 2013;123(3):1299-1309.
24. Iliff JJ, Wang M, Liao Y, Plogg BA, Peng W, Gundersen GA, Benveniste H, Vates GE, Deane R, Goldman SA, Nagelhus EA, Nedergaard M. A paravascular

pathway facilitates CSF flow through the brain parenchyma and the clearance of interstitial solutes, including amyloid beta. Science translational medicine 2012;4(147):147ra111.
25. Kress BT, Iliff JJ, Xia M, Wang M, Wei HS, Zeppenfeld D, Xie L, Kang H, Xu Q, Liew JA, Plog BA, Ding F, Deane R, Nedergaard M. Impairment of paravascular clearance pathways in the aging brain. Ann Neurol 2014;76(6):845-861.
26. Xie L, Kang H, Xu Q, Chen MJ, Liao Y, Thiyagarajan M, O'Donnell J, Christensen DJ, Nicholson C, Iliff JJ, Takano T, Deane R, Nedergaard M. Sleep drives metabolite clearance from the adult brain. Science 2013;342(6156):373-377.
27. Iliff JJ, Chen MJ, Plog BA, Zeppenfeld DM, Soltero M, Yang L, Singh I, Deane R, Nedergaard M. Impairment of glymphatic pathway function promotes tau pathology after traumatic brain injury. J Neurosci 2014;34(49):16180-16193.
28. Iliff JJ, Wang M, Zeppenfeld DM, Venkataraman A, Plog BA, Liao Y, Deane R, Nedergaard M. Cerebral arterial pulsation drives paravascular CSF-interstitial fluid exchange in the murine brain. J Neurosci 2013;33(46):18190-18199.
29. Ma Q, Ineichen BV, Detmar M, Proulx ST. Outflow of cerebrospinal fluid is predominantly through lymphatic vessels and is reduced in aged mice. Nature communications 2017;8(1):1434.
30. Goulay R, Flament J, Gauberti M, Naveau M, Pasquet N, Gakuba C, Emery E, Hantraye P, Vivien D, Aron-Badin R, Gaberel T. Subarachnoid Hemorrhage Severely Impairs Brain Parenchymal Cerebrospinal Fluid Circulation in Nonhuman Primate. Stroke 2017;48(8):2301-2305.
31. Lee H, Xie L, Yu M, Kang H, Feng T, Deane R, Logan J, Nedergaard M, Benveniste H. The Effect of Body Posture on Brain Glymphatic Transport. J Neurosci 2015;35(31):11034-11044.
32. Lee H, Mortensen K, Sanggaard S, Koch P, Brunner H, Quistorff B, Nedergaard M, Benveniste H. Quantitative Gd-DOTA uptake from cerebrospinal fluid into rat brain using 3D VFA-SPGR at 9.4T. Magn Reson Med 2018;79(3):1568-1578.
33. Taoka T, Naganawa S. Glymphatic imaging using MRI. J Magn Reson Imaging 2020;51(1):11-24.
34. Gaberel T, Gakuba C, Goulay R, Martinez De Lizarrondo S, Hanouz JL, Emery E, Touze E, Vivien D, Gauberti M. Impaired glymphatic perfusion after strokes revealed by contrast-enhanced MRI: a new target for fibrinolysis? Stroke 2014;45(10):3092-3096.
35. Ringstad G, Eide PK. Cerebrospinal fluid tracer efflux to parasagittal dura in humans. Nature communications 2020;11(1):354.
36. Ma Q, Schlegel F, Bachmann SB, Schneider H, Decker Y, Rudin M, Weller M, Proulx ST, Detmar M. Lymphatic outflow of cerebrospinal fluid is reduced in glioma. Scientific reports 2019;9(1):14815.

37. Magdoom KN, Brown A, Rey J, Mareci TH, King MA, Sarntinoranont M. MRI of Whole Rat Brain Perivascular Network Reveals Role for Ventricles in Brain Waste Clearance. Scientific reports 2019;9(1):11480.
38. Boxerman JL, Hamberg LM, Rosen BR, Weisskoff RM. MR contrast due to intravascular magnetic susceptibility perturbations. Magn Reson Med 1995;34(4):555.
39. Weisskoff RM, Zuo CS, Boxerman JL, Rosen BR. Microscopic susceptibility variation and transverse relaxation: theory and experiment. Magn Reson Med 1994;31(6):601.
40. Cao D, Kang N, Pillai JJ, Miao X, Paez A, Xu X, Xu J, Li X, Qin Q, Van Zijl PCM, Barker P, Hua J. Fast whole brain MR imaging of dynamic susceptibility contrast changes in the cerebrospinal fluid (cDSC MRI). Magn Reson Med 2020;84(6):3256-3270.
41. Absinta M, Vuolo L, Rao A, Nair G, Sati P, Cortese IC, Ohayon J, Fenton K, Reyes-Mantilla MI, Maric D, Calabresi PA, Butman JA, Pardo CA, Reich DS. Gadolinium-based MRI characterization of leptomeningeal inflammation in multiple sclerosis. Neurology 2015;85(1):18-28.
42. Naganawa S, Ito R, Kawai H, Taoka T, Yoshida T, Sone M. Confirmation of Age-dependence in the Leakage of Contrast Medium around the Cortical Veins into Cerebrospinal Fluid after Intravenous Administration of Gadolinium-based Contrast Agent. Magnetic resonance in medical sciences : MRMS : an official journal of Japan Society of Magnetic Resonance in Medicine 2020;19(4):375-381.
43. Albayram MS, Smith G, Tufan F, Tuna IS, Bostanciklioglu M, Zile M, Albayram O. Non-invasive MR imaging of human brain lymphatic networks with connections to cervical lymph nodes. Nature communications 2022;13(1):203.
44. Elster AD, Sobol WT, Hinson WH. Pseudolayering of Gd-DTPA in the urinary bladder. Radiology 1990;174(2):379-381.
45. Deshmane A, Gulani V, Griswold MA, Seiberlich N. Parallel MR imaging. J Magn Reson Imaging 2012;36(1):55-72.
46. Pruessmann KP, Weiger M, Scheidegger MB, Boesiger P. SENSE: sensitivity encoding for fast MRI. Magn Reson Med 1999;42(5):952-962.
47. Liang D, Liu B, Wang J, Ying L. Accelerating SENSE using compressed sensing. Magn Reson Med 2009;62(6):1574-1584.
48. Liang D, Liu B, Ying L. Accelerating sensitivity encoding using compressed sensing. Conf Proc IEEE Eng Med Biol Soc 2008;2008:1667-1670.
49. Basha TA, Akçakaya M, Goddu B, Berg S, Nezafat R. Accelerated three-dimensional cine phase contrast imaging using randomly undersampled echo planar imaging with compressed sensing reconstruction. NMR Biomed 2015;28(1):30-39.

50. Chatnuntawech I, Gagoski B, Bilgic B, Cauley SF, Setsompop K, Adalsteinsson E. Accelerated. Magn Reson Med 2015;74(1):13-24.
51. Cho SJ, Choi YJ, Chung SR, Lee JH, Baek JH. High-resolution MRI using compressed sensing-sensitivity encoding (CS-SENSE) for patients with suspected neurovascular compression syndrome: comparison with the conventional SENSE parallel acquisition technique. Clin Radiol 2019;74(10):817.e819-817.e814.
52. Heo HY, Zhang Y, Lee DH, Jiang S, Zhao X, Zhou J. Accelerating chemical exchange saturation transfer (CEST) MRI by combining compressed sensing and sensitivity encoding techniques. Magn Reson Med 2017;77(2):779-786.
53. Kawai N, Goshima S, Noda Y, Kajita K, Kawada H, Tanahashi Y, Nagata S, Matsuo M. Gadoxetic acid-enhanced dynamic magnetic resonance imaging using optimized integrated combination of compressed sensing and parallel imaging technique. Magn Reson Imaging 2019;57:111-117.
54. Nam JG, Lee JM, Lee SM, Kang HJ, Lee ES, Hur BY, Yoon JH, Kim E, Doneva M. High Acceleration Three-Dimensional T1-Weighted Dual Echo Dixon Hepatobiliary Phase Imaging Using Compressed Sensing-Sensitivity Encoding: Comparison of Image Quality and Solid Lesion Detectability with the Standard T1-Weighted Sequence. Korean J Radiol 2019;20(3):438-448.
55. Neuhaus E, Weiss K, Bastkowski R, Koopmann J, Maintz D, Giese D. Accelerated aortic 4D flow cardiovascular magnetic resonance using compressed sensing: applicability, validation and clinical integration. J Cardiovasc Magn Reson 2019;21(1):65.
56. Zong X, Lee J, John Poplawsky A, Kim SG, Ye JC. Compressed sensing fMRI using gradient-recalled echo and EPI sequences. Neuroimage 2014;92:312-321.
57. Morita K, Nakaura T, Maruyama N, Iyama Y, Oda S, Utsunomiya D, Namimoto T, Kitajima M, Yoneyama M, Yamashita Y. Hybrid of Compressed Sensing and Parallel Imaging Applied to Three-dimensional Isotropic T. Magn Reson Med Sci 2020;19(1):48-55.
58. Lohöfer FK, Kaissis GA, Müller-Leisse C, Franz D, Katemann C, Hock A, Peeters JM, Rummeny EJ, Karampinos D, Braren RF. Acceleration of chemical shift encoding-based water fat MRI for liver proton density fat fraction and T2* mapping using compressed sensing. PLoS One 2019;14(11):e0224988.
59. Moghari MH, Uecker M, Roujol S, Sabbagh M, Geva T, Powell AJ. Accelerated whole-heart MR angiography using a variable-density poisson-disc undersampling pattern and compressed sensing reconstruction. Magn Reson Med 2018;79(2):761-769.
60. Suh CH, Jung SC, Lee HB, Cho SJ. High-Resolution Magnetic Resonance Imaging Using Compressed Sensing for Intracranial and Extracranial Arteries: Comparison with Conventional Parallel Imaging. Korean J Radiol 2019;20(3):487-497.

61. Cao D, Kang N, Pillai JJ, Miao X, Paez A, Xu X, Xu J, Li X, Qin Q, Van Zijl PCM, Barker P, Hua J. Fast whole brain MR imaging of dynamic susceptibility contrast changes in the cerebrospinal fluid (cDSC MRI). Magn Reson Med 2020.
62. Lu H, Golay X, Pekar JJ, Van Zijl PC. Functional magnetic resonance imaging based on changes in vascular space occupancy. Magn Reson Med 2003;50(2):263-274.
63. Hua J, Qin Q, van Zijl PC, Pekar JJ, Jones CK. Whole-brain three-dimensional T2-weighted BOLD functional magnetic resonance imaging at 7 Tesla. Magn Reson Med 2014;72(6):1530-1540.
64. Miao X, Wu Y, Liu D, Jiang H, Woods D, Stern MT, Blair NIS, Airan RD, Bettegowda C, Rosch KS, Qin Q, van Zijl PCM, Pillai JJ, Hua J. Whole-Brain Functional and Diffusion Tensor MRI in Human Participants with Metallic Orthodontic Braces. Radiology 2020;294(1):149-157.
65. Horska A, Calhoun VD, Bradshaw DH, Barker PB. Rapid method for correction of CSF partial volume in quantitative proton MR spectroscopic imaging. Magn Reson Med 2002;48(3):555-558.
66. Qin Q. A simple approach for three-dimensional mapping of baseline cerebrospinal fluid volume fraction. Magn Reson Med 2011;65(2):385-391.
67. Weigel M, Hennig J. Contrast behavior and relaxation effects of conventional and hyperecho-turbo spin echo sequences at 1.5 and 3 T. Magn Reson Med 2006;55(4):826-835.
68. Duong TQ, Yacoub E, Adriany G, Hu X, Ugurbil K, Kim SG. Microvascular BOLD contribution at 4 and 7 T in the human brain: gradient-echo and spin-echo fMRI with suppression of blood effects. Magn Reson Med 2003;49(6):1019-1027.
69. Lustig M, Donoho D, Pauly JM. Sparse MRI: The application of compressed sensing for rapid MR imaging. Magn Reson Med 2007;58(6):1182-1195.
70. Rooney WD, Johnson G, Li X, Cohen ER, Kim SG, Ugurbil K, Springer CS, Jr. Magnetic field and tissue dependencies of human brain longitudinal 1H2O relaxation in vivo. Magn Reson Med 2007;57(2):308-318.
71. Zhang X, Petersen ET, Ghariq E, De Vis JB, Webb AG, Teeuwisse WM, Hendrikse J, van Osch MJ. In vivo blood T(1) measurements at 1.5 T, 3 T, and 7 T. Magn Reson Med 2013;70(4):1082-1086.
72. Wright PJ, Mougin OE, Totman JJ, Peters AM, Brookes MJ, Coxon R, Morris PE, Clemence M, Francis ST, Bowtell RW, Gowland PA. Water proton T1 measurements in brain tissue at 7, 3, and 1.5 T using IR-EPI, IR-TSE, and MPRAGE: results and optimization. MAGMA 2008;21(1-2):121-130.
73. Spijkerman JM, Petersen ET, Hendrikse J, Luijten P, Zwanenburg JJM. T 2 mapping of cerebrospinal fluid: 3 T versus 7 T. MAGMA 2018;31(3):415-424.

74. Liu P, Chalak LF, Krishnamurthy LC, Mir I, Peng SL, Huang H, Lu H. T1 and T2 values of human neonatal blood at 3 Tesla: Dependence on hematocrit, oxygenation, and temperature. Magn Reson Med 2016;75(4):1730-1735.
75. Cox EF, Gowland PA. Measuring T2 and T2' in the brain at 1.5T, 3T and 7T using a hybrid gradient echo-spin echo sequence and EPI. 2008; Toronto, Canada. p 1411.
76. Rohrer M, Bauer H, Mintorovitch J, Requardt M, Weinmann HJ. Comparison of magnetic properties of MRI contrast media solutions at different magnetic field strengths. Invest Radiol 2005;40(11):715-724.
77. Krishnamurthy LC, Liu P, Xu F, Uh J, Dimitrov I, Lu H. Dependence of blood T(2) on oxygenation at 7 T: in vitro calibration and in vivo application. Magn Reson Med 2014;71(6):2035-2042.
78. Nakada T, Kwee IL. Fluid Dynamics Inside the Brain Barrier: Current Concept of Interstitial Flow, Glymphatic Flow, and Cerebrospinal Fluid Circulation in the Brain. The Neuroscientist : a review journal bringing neurobiology, neurology and psychiatry 2019;25(2):155-166.
79. Klarica M, Rados M, Oreskovic D. The Movement of Cerebrospinal Fluid and Its Relationship with Substances Behavior in Cerebrospinal and Interstitial Fluid. Neuroscience 2019;414:28-48.
80. Benveniste H, Liu X, Koundal S, Sanggaard S, Lee H, Wardlaw J. The Glymphatic System and Waste Clearance with Brain Aging: A Review. Gerontology 2019;65(2):106-119.
81. Brinker T, Stopa E, Morrison J, Klinge P. A new look at cerebrospinal fluid circulation. Fluids and barriers of the CNS 2014;11:10.
82. Hladky SB, Barrand MA. Mechanisms of fluid movement into, through and out of the brain: evaluation of the evidence. Fluids and barriers of the CNS 2014;11(1):26.
83. Bedussi B, Almasian M, de Vos J, VanBavel E, Bakker EN. Paravascular spaces at the brain surface: Low resistance pathways for cerebrospinal fluid flow. J Cereb Blood Flow Metab 2018;38(4):719-726.
84. Fujima N, Kudo K, Tsukahara A, Yoshida D, Sakashita T, Homma A, Tha KK, Shirato H. Measurement of tumor blood flow in head and neck squamous cell carcinoma by pseudo-continuous arterial spin labeling: comparison with dynamic contrast-enhanced MRI. J Magn Reson Imaging 2015;41(4):983-991.
85. Li KL, Zhu XP, Waterton J, Jackson A. Improved 3D quantitative mapping of blood volume and endothelial permeability in brain tumors. J Magn Reson Imaging 2000;12(2):347-357.
86. Crescenzi R, Donahue PM, Braxton VG, Scott AO, Mahany HB, Lants SK, Donahue MJ. 3.0 T relaxation time measurements of human lymph nodes in

adults with and without lymphatic insufficiency: Implications for magnetic resonance lymphatic imaging. NMR Biomed 2018;31(12):e4009.
87. McKnight CD, Rouleau RM, Donahue MJ, Claassen DO. The Regulation of Cerebral Spinal Fluid Flow and Its Relevance to the Glymphatic System. Current neurology and neuroscience reports 2020;20(12):58.
88. van Zijl PC, Eleff SM, Ulatowski JA, Oja JM, Ulug AM, Traystman RJ, Kauppinen RA. Quantitative assessment of blood flow, blood volume and blood oxygenation effects in functional magnetic resonance imaging. Nat Med 1998;4(2):159-167.
89. Knutsson L, Stahlberg F, Wirestam R. Absolute quantification of perfusion using dynamic susceptibility contrast MRI: pitfalls and possibilities. MAGMA 2010;23(1):1-21.
90. Su P, Fan H, Liu P, Li Y, Qiao Y, Hua J, Lin D, Jiang D, Pillai JJ, Hillis AE, Lu H. MR fingerprinting ASL: Sequence characterization and comparison with dynamic susceptibility contrast (DSC) MRI. NMR Biomed 2020;33(1):e4202.
91. Bell LC, Does MD, Stokes AM, Baxter LC, Schmainda KM, Dueck AC, Quarles CC. Optimization of DSC MRI Echo Times for CBV Measurements Using Error Analysis in a Pilot Study of High-Grade Gliomas. AJNR Am J Neuroradiol 2017;38(9):1710-1715.
92. Newton AT, Pruthi S, Stokes AM, Skinner JT, Quarles CC. Improving Perfusion Measurement in DSC-MR Imaging with Multiecho Information for Arterial Input Function Determination. AJNR Am J Neuroradiol 2016;37(7):1237-1243.
93. Quarles CC, Gore JC, Xu L, Yankeelov TE. Comparison of dual-echo DSC-MRI- and DCE-MRI-derived contrast agent kinetic parameters. Magn Reson Imaging 2012;30(7):944-953.
94. Sourbron S, Heilmann M, Biffar A, Walczak C, Vautier J, Volk A, Peller M. Bolus-tracking MRI with a simultaneous T1- and T2*-measurement. Magn Reson Med 2009;62(3):672-681.
95. Stokes AM, Semmineh N, Quarles CC. Validation of a T1 and T2* leakage correction method based on multiecho dynamic susceptibility contrast MRI using MION as a reference standard. Magn Reson Med 2016;76(2):613-625.
96. Jochimsen TH, Newbould RD, Skare ST, Clayton DB, Albers GW, Moseley ME, Bammer R. Identifying systematic errors in quantitative dynamic-susceptibility contrast perfusion imaging by high-resolution multi-echo parallel EPI. NMR Biomed 2007;20(4):429-438.
97. Newbould RD, Skare ST, Jochimsen TH, Alley MT, Moseley ME, Albers GW, Bammer R. Perfusion mapping with multiecho multishot parallel imaging EPI. Magn Reson Med 2007;58(1):70-81.
98. Paulson ES, Prah DE, Schmainda KM. Spiral Perfusion Imaging With Consecutive Echoes (SPICE) for the Simultaneous Mapping of DSC- and DCE-

MRI Parameters in Brain Tumor Patients: Theory and Initial Feasibility. Tomography 2016;2(4):295-307.
99. Schmiedeskamp H, Andre JB, Straka M, Christen T, Nagpal S, Recht L, Thomas RP, Zaharchuk G, Bammer R. Simultaneous perfusion and permeability measurements using combined spin- and gradient-echo MRI. J Cereb Blood Flow Metab 2013;33(5):732-743.
100. Schmiedeskamp H, Straka M, Newbould RD, Zaharchuk G, Andre JB, Olivot JM, Moseley ME, Albers GW, Bammer R. Combined spin- and gradient-echo perfusion-weighted imaging. Magn Reson Med 2012;68(1):30-40.
101. Skinner JT, Robison RK, Elder CP, Newton AT, Damon BM, Quarles CC. Evaluation of a multiple spin- and gradient-echo (SAGE) EPI acquisition with SENSE acceleration: applications for perfusion imaging in and outside the brain. Magn Reson Imaging 2014;32(10):1171-1180.
102. Stokes AM, Skinner JT, Quarles CC. Assessment of a combined spin- and gradient-echo (SAGE) DSC-MRI method for preclinical neuroimaging. Magn Reson Imaging 2014;32(10):1181-1190.
103. Stokes AM, Quarles CC. A simplified spin and gradient echo approach for brain tumor perfusion imaging. Magn Reson Med 2016;75(1):356-362.
104. Stokes AM, Skinner JT, Yankeelov T, Quarles CC. Assessment of a simplified spin and gradient echo (sSAGE) approach for human brain tumor perfusion imaging. Magn Reson Imaging 2016;34(9):1248-1255.

Biographical Sketch

Di Cao was born January 6th, 1994, in Xiangyang, Hubei province, China. Di Cao started his undergraduate studies at Tsinghua University in Beijing, China, in September 2012. He obtained his bachelor's degree in the Department of Engineering Physics from Tsinghua University in June 2016, where he developed a huge interest in MRI medical imaging. He also got a computer science miner degree from Tsinghua University in June 2016. He then joined the Biomedical Engineering Graduate Program at Johns Hopkins University to pursue his Ph.D. under the supervision of Dr. Jun Hua. He continued to perform research in the field of MRI dynamic imaging of cerebral lymphatic vessels. With the support of his mentor, committee members, lab mates, friends, and families, Di Cao completed his dissertation of "Contrast enhanced MRI for the measurement of dynamic signal changes in the CSF and cerebral lymphatic vessels" in 2022.